Available online at www.sciencedirect.com

SciVerse ScienceDirect

Procedia Engineering 00 (2012) 000–000

Procedia Engineering

www.elsevier.com/locate/procedia

5th BSME International Conference on Thermal Engineering

Numerical Simulation of Slag Foaming in High Temperature Molten Metal with Population Balance Modeling

M.A.Sattar*, J.Naser, G.Brooks

Faculty of Engineering and Industrial Science
Swinburne University of Technology
Hawthorn 3122- Australia

Abstract

A computational fluid dynamic (CFD) model has been developed for the simulation of slag foaming on bath smelting slag (CaO-SiO-Al_2O_3-FeO) by considering foam as a separate phase which is comprised of a mixture of gas and liquid. The model accounts for the formation of foam due to transformation of both gas and liquid into foam and it's destruction due to liquid drainage and bursting of bubbles. The bubble break-up and coalescence was considered in the gas-liquid dispersion whereas in the foam layer, the bubble coalescence due to film rupture was incorporated. Population balance modelling was used to track the number density of different bubble class. The model predicted the foam height of the slag system (CaO-SiO-Al_2O_3-FeO). The foam height was found to increase with the increase of superficial gas velocity. The content of FeO was changed and its effect on the foaming index was observed. The results from the present model show that foaming index decreases with increase of FeO content in slag. The results from the CFD model also show that the foaming index of a slag with Al_2O_3 is higher than that of slag without Al_2O_3. The predicted results from the present study are in reasonable agreement with the experimental data.

Keywords: Bubble break up; Coalescence; Film rupture; Population balance; CFD.

1. Introduction

Slag foaming phenomena are found in many ferrous and non-ferrous pyrometallurgical processes, such as electric arc furnace (EAF), basic oxygen furnace (BOF), direct ironmaking, and coppermaking. The pyrometallurgical processes generate large quantity of gas which causes slag foaming. Foaming slags are important for post combustion in direct ironmaking and the large surface areas facilitate the multiphase reactions; leading to improved process kinetics, heat transfer and energy efficiency [1-2]. On the other hand excessive slag foaming can cause the slag to overflow the vessel. This phenomenon is termed as slopping which reduces productivity and increases operating cost and in some cases damages the vessel. Therefore, it is important to understand the features of slag foaming in pyrometallurgical processes.

The foaming index, which correlates the foam height with superficial gas velocity, has been used for aqueous systems [3]. The foaming index has been empirically related to physical properties of slags such as the surface tension, viscosity, and density of the liquid and the size of the bubbles. Jiang and Fruehan [2] empirically modelled foaming for different slag

* Corresponding author. Tel.: +61424910627; fax: +61 3 9214 8264.
E-mail address: ssattar@swin.edu.au

system. Lahiri and Seetharaman [4] explicitly accounted for the bubble size of the foam. Ito and Fruehan [5] studied the foaming index and foam life to understand the effect of slag composition on foaming in iron and steel making process. They found that slag foaming increases with increasing viscosity and decreasing surface tension. At the same time they have found that suspended second particle stabilize the foam life and had a larger effect than that of viscosity and surface tension. The bubble break up model of Luo and Svendsen [6] and the coalescence model of Prince and Blanch [7] are used in the present study. The bubble coalescence model based on film rupture by Tong et al. [8] has been used in the foam layer. The advent of high speed computing machine facilitates the use of computational fluid dynamic model in many engineering fields. Numerous CFD model of multiphase flow have been developed, and numerical data has been validated through comparison with experimental data. It has been successfully used in metal processing involving gas-liquid flow [9-11].

In this study a CFD model based on Euler–Euler approach has been developed to simulate slag foaming. The model predicts the foam height with different superficial gas velocity and iron oxide (FeO) content. The foam was considered as separate phase which is comprised of a mixture of gas and liquid. Different bubble classes were considered and the population balance modeling was incorporated to track the number density of different bubble classes. Bubble break up and bubble coalescence were employed and their Sauter mean diameter were evaluated in the foam. Finally foaming index for different FeO content was determined, elucidated and compared to experimental data.

2. Mathematical model

2.1. Euler-Euler Multiphase model

The governing equations used in the present study under the Eulerian-Eulerian multiphase approach are summarized in this section. Gas, liquid and foam are treated as separate phases. The CFD solver employed uses the finite volume discretization method which rests on integral conservation statements applied to a general control volume. The Eulerian multiphase flow model solves the conservation of mass and momentum of each phase in each cell. The mass conversion equation used:

$$\frac{\partial \alpha_k \rho_k}{\partial t} + \nabla . \alpha_k \rho_k V_k = \sum_{l=1, l\neq k}^{N} \Gamma_{kl}\ , \quad k=1,\ldots\ldots,N \tag{1}$$

Where α_k is the volume fraction of phase k, V_k is phase k velocity, and Γ_{kl} is the interfacial mass exchange between phases k and l. The mass transformation between gas and foam was calculated using the following equation:

$$\Gamma_f = \frac{\pi}{6} d_i^3 (\rho_g \Sigma_i^n N_{i_g} - \rho_f \Sigma_i^n N_{i_f}) = -\Gamma_g \qquad N_{i_g} \leq N_{i_{av}} \tag{2}$$

Where N_{i_g} is the number of bubble in gas phase transformed into foam phase, N_{i_f} is the number of bubble in foam transformed into gas phase and $N_{i_{av}}$ is the number of gas bubble available in that cell. The number of gas bubble transformed into foam bubble was calculated from the equation.

$$N_{i_g} = \frac{\alpha_l v_c}{n_p a_p l_i} \tag{3}$$

Where α_l is volume fraction of liquid in the cell and v_c is the volume of that cell. The number of foam bubble transformed into gas bubble is calculated from the equation:

$$N_{i_f} = \frac{q_{PB}}{n_p a_p l_i} \tag{4}$$

The liquid drainage due to gravity through plateau border derived by Bhakta and Ruckenstein [12] is used in the present study.

$$q_{PB} = 2N\bar{R}\left(\frac{n_p}{5}\right)\bar{q} = \frac{3}{15} N R n_p a_p u \tag{5}$$

The mass transformation between liquid and foam was calculated using the following equation:

$$\Gamma_f = n_p a_p l_i(\rho_l \sum_i^n N_{i_g} - \rho_f \sum_i^n N_{i_f}) = -\Gamma_l \qquad N_{i_g} \leq N_{i_{av}} \tag{6}$$

The population balance equation has been used as:

$$\frac{\partial}{\partial t}\alpha_k \rho_k \emptyset_{ki} + \nabla.\alpha_k \rho_k V_k \emptyset_{ki} = +\nabla.\alpha_k \rho_k D_{ki} \nabla_{\emptyset_{ki}} + S_i \tag{7}$$

Where $S_i = B_{B_i} - D_{B_i} + B_{C_i} - D_{C_i}$ is the source term due to break up and coalescence in the foam and gas-liquid dispersion and $\emptyset_i$ is the fraction of bubble class i. B_{B_i}, B_{C_i} and D_{B_i}, D_{C_i} are birth and death due to break up and coalescence. The source term model of Hagesaether et al., [13] has been used with rectification as:

$$B_{B_i} = \sum_{k=i+1, i\neq N}^{N} \Omega_B(\vartheta_k, \vartheta_i) + \sum_{k=1, i\neq N}^{i} X_{i+1,k}\Omega_B(\vartheta_{i+1}, \vartheta_k), i = 1, \dots\dots, N, \tag{8}$$

$$D_{B_i} = \sum_{k=1}^{i-1} \Omega_B(\vartheta_i, \vartheta_k) + \sum_{k=1, i\neq N}^{i} X_{i,k}\Omega_B(\vartheta_i, \vartheta_k)\ i = 2, \dots\dots, N, \tag{9}$$

$$B_{C_i} = \sum_{j=1, i\neq N}^{i-1} X_{i,j}\Omega_C(\vartheta_i, \vartheta_j) + \sum_{j=1}^{i-1}(1 - X_{i-1,j})\Omega_C(\vartheta_{i-1}, \vartheta_j), i = 2, \dots\dots, N, \tag{10}$$

$$D_{C_i} = \sum_{j=1}^{N-1} \Omega_C(\vartheta_i, \vartheta_j) - \sum_{j=1}^{i} X_{i,j}\Omega_C(\vartheta_i, \vartheta_j), i = 1, \dots\dots, N-1, \tag{11}$$

Where $\Omega_B(\vartheta_k, \vartheta_i)$ is the break-up rate of bubble class k that goes into i and the complementery fraction $v_j = x_{i,k}v_i + (1 - x_{i,k})v_i$ and $x_{i,k} = 2^{1+k-i}, k < i$. The term $\Omega_C(\vartheta_i, \vartheta_j)$ is coalescecne rate of bubble i and j and the colaescence product is distributed as $v_i + v_j = x_{i,j}v_i + (1 - x_{i,j})v_{i+1}$ and $x_{i,j} = 1 - 2^{j-i}, i \geq j$.

2.2. Foam formation and destruction

In foam, bubble bursts at the top and coalesce inside due to film rupture caused by liquid drain-out through the plateau border. It is difficult to incorporate these characteristics of foam in an ordinary two phase gas/liquid simulation approach because the gas diffuses to the atmosphere and is difficult to hold at the top. The above drawback is eliminated by considering foam as a separate phase made up of gas and liquid. The new approach enables us to apply above characteristic of foam. In wet foam the liquid volume fraction is typically between 10% and 30% while in dry foam the volume fraction of liquid is less than 10% [14-16]. In the present study the gas liquid mixture is considered to be foam when the gas volume fraction is more than or equal to 0.75. The gas and liquid transformation mechanism is activated in the model when the gas fraction is 75% or above. However, the amount of gas and liquid transformed into foam and vice versa are governed by equations (2)-(6). That means, gas and liquid will not be transformed into foam just because the criteria of 75% gas in a cell is satisfied. However, in the absence of a proper surface active agent in the foam, the viscosity, density and surface tension properties of foam will be such that the bubble inside the foam will burst immediately and foam will return to liquid and gas phases. A total of 21 scalars were assigned to track 10 bubble classes in gas and 10 bubble classes in foam separately and a liquid in the foam. The density and viscosity of foam is calculated using the following equation:

$$\rho_f = \rho_g + \rho_l(1 - \emptyset) \tag{12}$$

$$\mu_f = \mu_g + \mu_l(1 - \emptyset) \quad (13)$$

Where ρ is density, μ is viscosity $\emptyset$ is liquid fraction in the foam and subscript f, g, l denote foam, gas and liquid respectively. The bubble is considered as pentagonal dodecahedron shape which consists of 12 films and 30 channels. The number of film per bubble is $n_f = 6$ and the number of plateau border channel is $n_p = 10$. The total amount of liquid entrapped per bubble is the sum of the liquid in lamellae and the plateau border. The total amount of liquid $\emptyset_i$ entrapped by the bubble class i is:

$$\emptyset_i = N_i n_p a_p l_i + N_i n_f a_f x_f \quad (14)$$

Where N_i is the number of bubble, l_i is the length of plateau border, a_p is the cross section of the plateau border of bubble class i and x_f is the thickness of the film. The thickness of the film is much smaller, so neglecting the liquid in film $\emptyset_i = N_i n_p a_p l_i$. Total amount of liquid entrapped by all the bubbles in a bubble class is the sum of the liquid entrapped by each individual bubbles in the class.

$$\emptyset = \sum_i^N \emptyset_i \quad (15)$$

The liquid drainage velocity $u = \frac{c_v a_p \rho g}{20\sqrt{3}\mu}$ due to gravity through plateau border derived by Bhakta and Ruckenstein [12] is used in the present model and the cross section of the plateau border is $a_p = 0.161 {r_p}^2$.

2.3. Bubble break up and coalescence model

The break up model of Luo and Svendsen [6] was used in the present study. The rate of bubble break up Ω_B is the product of collision frequency ω_B and the probability of bubble break up P_B. The break up rate of bubble class i into j colliding with the eddy size λ_j can be written as:

$$\Omega_B(\vartheta_k, \lambda_j, \vartheta_i) = \omega_B(d_i, \lambda_j) \times P_B(d_i, \lambda_j, d_k) \quad (16)$$

The coalescence model of Prince and Blanch [7] has been used in the present study. The turbulent collision rate equation used was:

$$\theta_{ij}^T = 0.089 n_i n_j (d_i + d_j)^2 \varepsilon^{1/3} (d_i^{2/3} + d_j^{2/3})^{1/2} \quad (17)$$

The laminar shear collision rate:

$$\theta_{ij}^{LS} = \frac{4}{3} n_i n_j (r_i + r_j)^3 \left(\frac{\overline{dU_l}}{dR}\right) \quad (18)$$

The mean shear rate is calculated by:

$$\bar{\gamma}(R) = 5.3 \frac{U_{l,max}}{R_T} \quad (19)$$

Where R_T is the radius of the container, $U_{l,max} = \left(\frac{(1-0.75\alpha_g)}{1-\alpha_g}\right)\frac{\alpha_g g D_T^2}{48 \upsilon_t}$ is the centerline liquid circulation velocity and $\upsilon_t = 0.0536 \frac{D_T^{1.77}}{\rho_l}$ is the turbulent kinetic viscosity. The coalescence efficiency $P_C(r_i, r_j) = exp\left[-\frac{\left\{\frac{r_{ij}^3 \rho_l}{16\sigma}\right\}^{1/2} \varepsilon^{1/3} \ln\frac{h_0}{h_f}}{r_{ij}^{2/3}}\right]$ with initial and final thickness for air-water is 1×10^{-4}m and 1×10^{-8}m from Prince and Blanch [6]. The coalescence rate Γ_{ij} of bubble i and j is given by the total collision frequency multiplied by the coalescence efficiency.

$$\Gamma_{ij} = \{\theta_{ij}^T + \theta_{ij}^{LS}\} \times P_C(r_i, r_j) \quad (20)$$

The coalescence rate $\Omega^f_{C_{i,j}}$ of a bubble of the ith group with bubbles of the jth group in the foam is [8]:

$$\Omega^f_{C_{i,j}} = n_{p_i} P_{i,j} f_{i,j} \tag{21}$$

where n_{p_i} is the number of films per bubble of the ith group, $P_{i,j} = k\frac{1}{\tau}$ is the failure rate of films separating bubbles of the ith and jth groups, $f_{i,j} = \frac{n_{p_i} n_i}{\sum_{j=1}^{M} n_{p_j} n_j}$ is the probability of a bubble of the ith group sharing the same film with the bubbles of jth group in the foam. n_i and n_j is the number of bubble of the ith and jth group respectively. Amount of liquid per bubble, $\emptyset_i/d_i$ so the time required to drain out this liquid is $\tau = (\emptyset_i/d_i)/q_{pB}$.The foaming index was calculated using the equation from Ito and Fruehan [5] as:

$$\sum = \frac{H_f}{U_g^s} \tag{22}$$

Where H_f is the foam height (cm) from the liquid surface and $U_g^s$is the superficial gas velocity (cm/s).

3. Model geometry and methodology

The predictions were carried in a container of height 12cm and the diameter of 4.5cm simulating the small scale experimental model of Jiang and Fruehan [2]. Two different grid of the model was generated with a control volume of 207,705 and 150,103. Simulation was performed on both grid using superficial gas velocity of 1cm/s. and it has been verified the convergence of the solution in both cases. No significant differences were observed in the results. Therefore, for all the subsequent simulations, the 150,103 control volumes numerical mesh was used. The generated grid for the present model is presented in Figure 1. The nozzle with diameter of 1.6mm was placed at centre and 1cm above from the bottom. As no experimental data for the initial bubble diameter issued from the nozzle were available, the Argon (Ar) gas was assumed to enter the calculation domain as bubbles of diameter of 0.5mm. When the flow dynamics and foam height reached a quasi-steady state, the height of foam was measured as the distance between the top surface of the clear liquid and the top surface of the foam. The simulation was performed by commercial CFD solver in AVL FIRE 2009.2 [17], but the full foaming model comprising of eqns. (1)-(22) were incorporated as subroutine written by the author in FORTRAN.

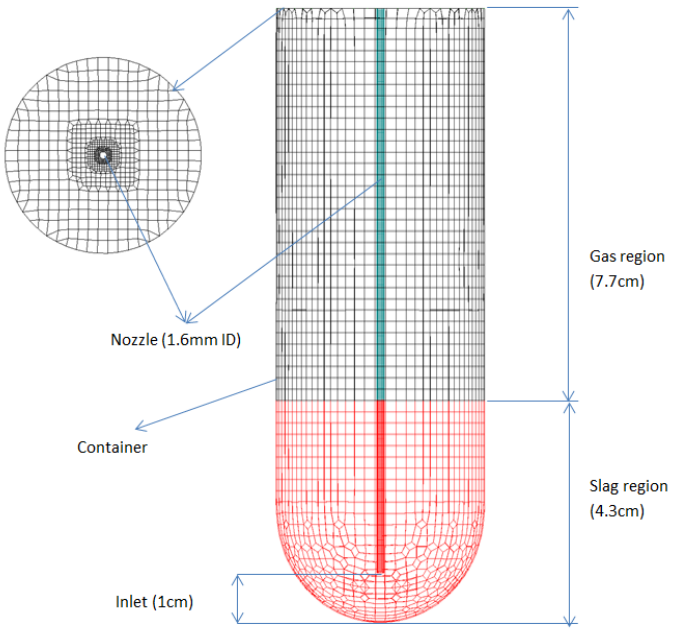

Fig. 1. Grid generated for the simulation

In this model, an unsteady state solution for multiphase momentum and continuity were obtained and for turbulence, a standard $k-\varepsilon$ turbulence model was used. For momentum and turbulence, first order upwind differencing scheme was used whereas central differencing scheme with second order accuracy was used for the continuity equation. The properties of the fluids used in this study are presented in Table 1.

Table 1. The properties of the fluids modelled.

Properties	Gas(Ar)	Liquid CaO/SiO=1.25, Pct Al_2O_3=4			Foam
		Pct FeO =3.0	Pct FeO =7.5	Pct FeO=15	
Density(kg/m^3)	0.2745	2733	2790	2889	Eq.(12)
Viscosity(Ns/m^2)	2.23E-05	0.381	0.353	0.314	Eq.(13)
Surface tension (mN/M)	-	477.2	483.6	494.6	-

4. Results and discussion

The simulation was carried out in a crucible filled up to 4cm of slag from the bottom. The simulation was run for 300 second of real time. Due to transient flow behaviour, the foam height was in quasi steady state so the average foam heights from 250s to 300s were measured at an interval of 10s. The foam heights at different position were measured and the average height of foam was considered. The instantaneous foaming heights are presented as foam volume fraction for superficial gas velocity of 1, 2 and 3cm/s at 250s in Figure 3.

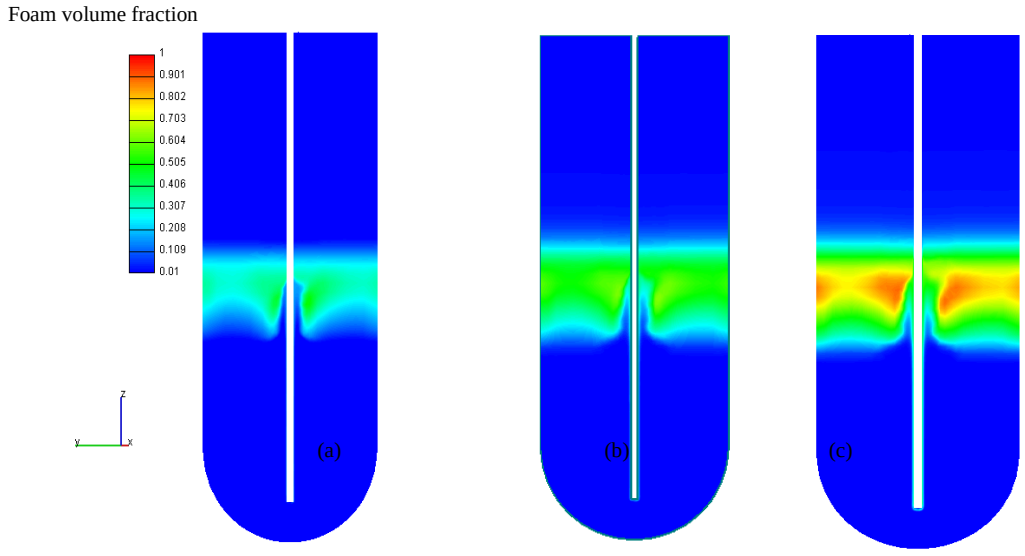

Fig. 3. Slag foam formation at 1773K for 3pct FeO (a) $U_g = 1cm/s$ (b) $U_g = 2cm/s$ (c) $U_g = 3cm/s$.

Different superficial gas velocities were studied for the same composition to achieve accurate foaming index. The foaming height of CaO-SiO-Al_2O_3-FeO slags as a function of superficial gas velocity is shown in Figure 4 along with the data from Jiang and Fruehan [2]. As expected the foaming height increases with the increase of gas flow rate when the slag composition is same.

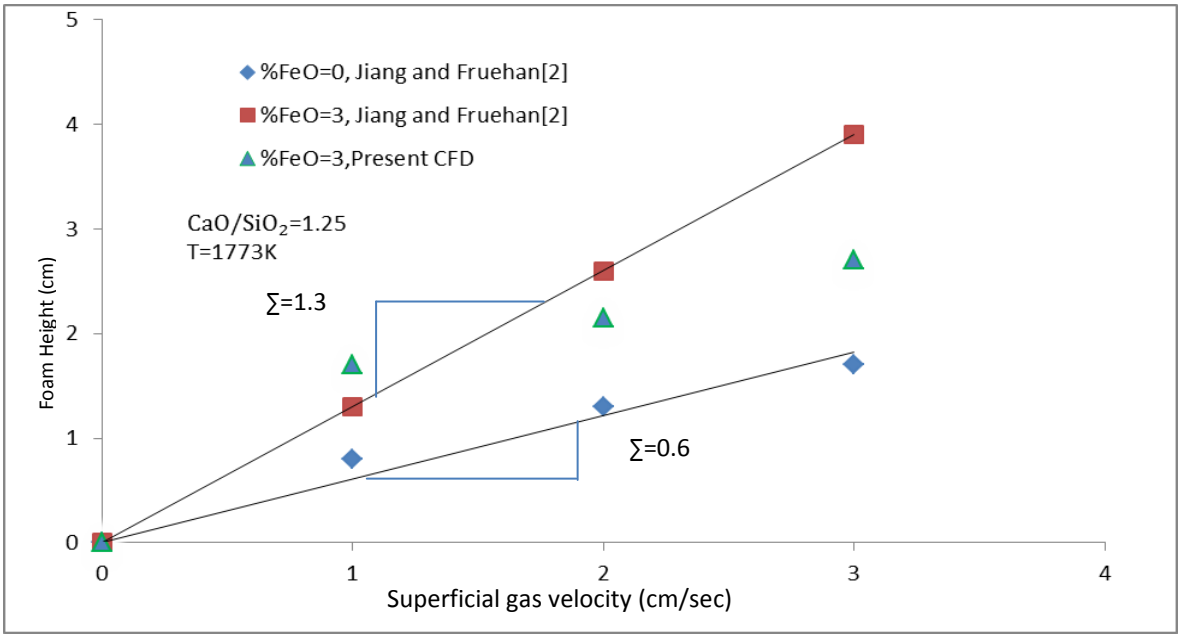

Fig.4. Foam heights of slags with different superficial gas velocity at 1773K.

In this model the height of slag foam depends on the foam formation due to gas flow and destruction due to the bubble burst at the top and the liquid drainage. The liquid drainage through plateau border channel remained the same for the same slag composition but the total liquid drainage in the foam increases due to the increases of volume of foam. Bubble burst at the top which remain constant due to constant surface area. For this reason increasing superficial gas velocity causes the increases of foam height when the slag composition is same. The foaming index of the present CFD model was measured as 1.24 from the slope of the Figure 4 for slag with FeO 3pct. The foaming indices from the present CFD and from Jiang and Fruehan [2] as well as the predicted data from Ito and Fruehan [5] are presented in Figure 5.

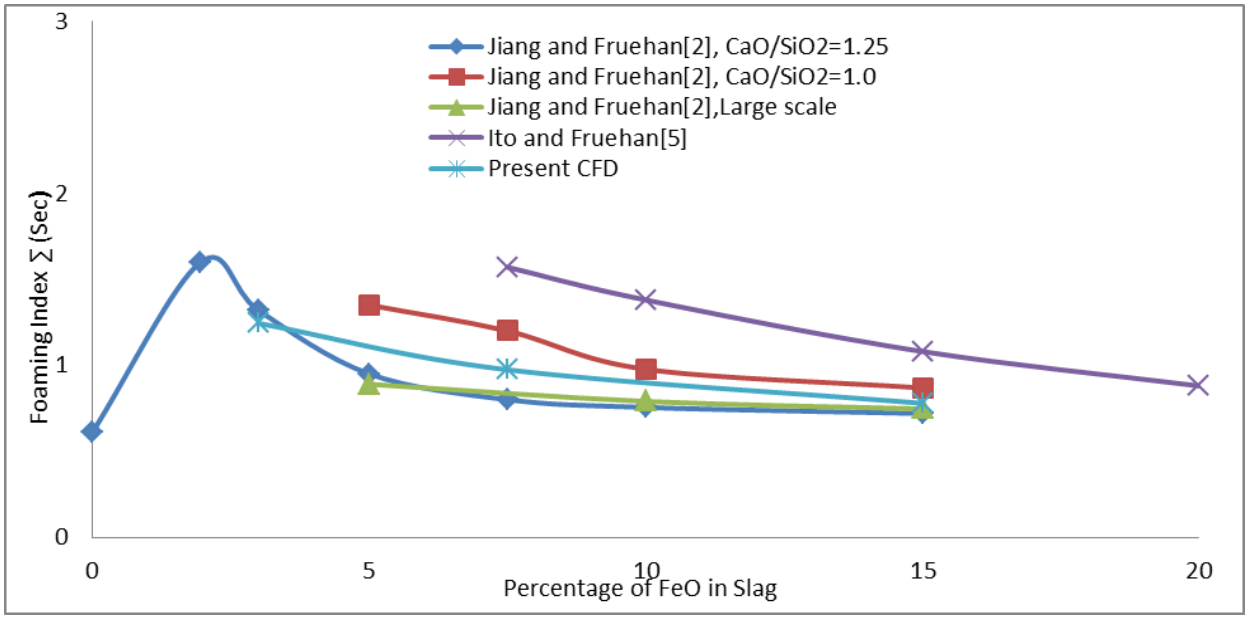

Fig.5. Foaming index of slag for different composition at 1773K.

It can be seen from the Figure 5 that in all cases the foaming index decreases with increase of FeO (For Jiang and Fruehan[2] when pct FeO>2). The foaming index increases with viscosity and is inversely proportional to the square root of

surface tension [5]. The net result for these slags is that foaming index decreases with increasing the FeO content (Jiang and Fruehan [2]). The above phenomena can be attributed to the fact that increasing FeO in slag decreases the viscosity of the slag (see Table 1). The drainage of liquid in foam increases with decreases of viscosity. So the height of foam decreases thus decreases the foaming index. The figure also shows that the foaming index of slag with Al_2O_3 is higher than that of slag without Al_2O_3. This is because Al_2O_3 increase the viscosity of slag [2]. The increase of viscosity increases the foaming index as mentioned above. With the 0.5mm diameter of bubble assumed to enter into calculation domain from the nozzle, the Sauter mean diameter calculated in the foam are 0.77mm, 0.85mm and 0.95mm when the FeO content is 3, 7.5 and 15 percent respectively. The above phenomena can be attributed to the fact that increasing FeO in slag decreases the viscosity of the slag (see Table 1). The drainage of liquid in foam increases with the decreases of viscosity. The rate of film rupture increases with the increased drainage causing an increase in the number of upper bubble classes and the Sauter mean diameter.

The results of the present CFD model are in reasonably good agreement with the experimental data of Jiang and Fruehan [2]. The computed foaming index of the present CFD was 5.75% less than that of Jiang and Fruehan [2] when FeO was 3pct. On the other hand the computed foaming indices of the present CFD were 21.77% and 8.35% more than that of Jiang and Fruehan [2] when FeO were 7.5pct and 15pct respectively. The present CFD model assumes that the shape of bubbles during the formation of foam is pentagonal dodecahedron but in reality the bubbles of different shapes exist in the foam. It is also considered in the present simulation that the cross section of the plateau border channel does not change with height of foam and the liquid in the lamellae is negligible compared to the plateau border channel. The life of foam depends on the concentration of surface active agent in the foam. The concentration gradient of the surface active agent in the foam is important for the calculation of drainage and film rupture. At the same time numerical inaccuracy associated with the numerical schemes used in the present study and the turbulence model used in the present study may also have contributed to the inaccuracies in the results. The discrepancies between the results from the present CFD model and that of the experimental data can be attributed to the above mentioned facts. More experiment results based on the above phenomena are necessary to incorporate the physics of foaming in the present CFD model for accurate prediction of the features of foam.

5. Conclusions

In this study a CFD model has been developed for the simulation of slag foaming on bath smelting slag. The results from the present CFD model show that foaming index decreases with increase of FeO content in slag. This phenomenon was attributed to the fact that increasing FeO in slag decreases the viscosity but increases the surface tension. The drainage of liquid in foam increases with the decreases of viscosity resulting in a decrease of foaming index. The results from the CFD model also showed that the foaming index of a slag with Al_2O_3 is higher than that of slag without Al_2O_3.The reason behind this was identified as the increases of viscosity due to addition of Al_2O_3. The Sauter mean diameter is found to increases with increases of FeO content in slag. This was attributed to the fact that the drainage of liquid in foam increases with the decreases of viscosity. The increased drainage leads to increased rate of film rupture and the number of upper bubble class increases thus causing the Sauter mean diameter to increase. The predicted results from the present study are in reasonably good agreement with the experimental data. The reasons of discrepancies between results of the present CFD model and that of the experimental data were due to the assumptions made to avoid the complexity of simulation and numerical schemes and turbulence model used.

References

[1] Nexhip C, Shouyi S., and Jahanshahi S., 2004. Physicochemical properties of foaming slags. International Materials Reviews 49(5), p.286-298.
[2] Jiang R., and Fruehan R.J.,1991. Slag foaming in bath smelting. Metallurgical and Materials Transactions B 22B, p.481-489.
[3] Bikerman J.J., 1953.Foams: Theory and industrial application, Reinhold Publishing Corporation, New York, NY, p.37.
[4] Lahiri A.K., and Seetharaman S.,2002. Foaming Behavior of Slags. Metallurgical and Materials Transactions B, 33B, p.499-502.
[5] Ito K., and Fruehan R.J.,1989.Study on the Foaming of CaO-SiO2-FeO Slags: Part I. Foaming Parameters and Experimental Results. Metallurgical and Materials Transactions B 20B,p.509-14.
[6] Luo H., Svendsen H.F.,1996. Theoretical model for drop and bubble breakup in turbulent dispersions. A.I.Ch.E. Journal42, p.1225-1233.
[7] Prince M.J., Blanch, H.W.,1990. Bubble coalescence and break-up in air-sparged bubble columns. A.I.Ch.E. Journal36, p.1485-1499.

[8] Tong M.K., Cole K., Neethling S.J.,2011. Drainage and stability of 2D foams: Foam behaviour in vertical Hele-Shaw cells. Colloids and Surfaces A: Physicochem. Eng. Aspects 382,p.42–49.
[9] Alam M., Naser J., Brooks G.,2010. Computational Fluid Dynamics Modeling of Supersonic Coherent Jets for Electric Arc Furnace Steelmaking Process. Metallurgical and Materials Transactions B 41b,p.1354-1367.
[10] Alam M., Naser J., Brooks G., Fontana A.,2012. Computational Fluid Dynamics Model of Shrouded Supersonic Jet Impingement on a Water Surface. ISIJ International 52(6).
[11] Huda N., Naser J., Brooks G., Reuter M., Matusewicz R., 2011. Computational Fluid Dynamic Modeling of Zinc Slag Fuming Process in Top-Submerged Lance Smelting Furnace.Metallurgical and Materials Transactions BDOI: 10.1007/s11663-011-9558-6, 2011
[12] Bhakta A., Ruckenstein E.,1997. Decay of standing foams drainage coalescence and collapse. Advances in Colloid and Interface Science70, p.1-124.
[13] Hagesaether L., Jakobsen H.A., Svendsen H.F.,2002. A model for turbulent binary breakup of dispersed fluid particles. Chemical Engineering Science57(16),p.3251-3267.
[14] Pawlat J., Hayashi N., Ihara S., Satoh S., Yamabe C., Pollo. I.,2004. Foaming column with a dielectric covered plate-to-metal plate electrode as an oxidants' generator. Advance in Environmental Research8, p.351-358.
[15] Pilon L., Viskanta R., 2004. Minimum superficial gas velocity for onset of foaming. Chemical Engineering and Processing43, p.149-160.
[16] Drenckhan W., Langevin D., 2010. Monodisperse foams in one to three dimensions. Current Opinion in Colloid & Interface Science15, p.341-358.
[17] AVL FIRE v2009.2. AVL LIST GmbH, Graz, Austria.

Available online at www.sciencedirect.com

SciVerse ScienceDirect

Procedia Engineering 00 (2012) 000–000

Procedia Engineering

www.elsevier.com/locate/procedia

5th BSME International Conference on Thermal Engineering

Characteristics of condensing flows in shear layer of axisymmetric supersonic jets

Junji Nagao[a], Shigeru Matsuo[b]*, Tokitada Hashimoto[b], Toshiaki Setoguchi[c], Md. Tawhidul Islam Khan[b] and Heuy Dong Kim[d]

[a]Graduate School of Science & Engineering, Saga University, 1 Honjo-machi, Saga-shi, Saga 840-8502, Japan
[b]Department of Advanced Technology Fusion, Saga University, 1 Honjo-machi, Saga 840-8502, Japan
[c]Institute of Ocean Energy, Saga University, 1 Honjo-machi, Saga-shi, Saga 840-8502, Japan
[d]School of Mechanical Engineering, Andong National University, 388 Song Cheon Dong, Andong 760-749, Korea

Abstract

When the high pressure gas is exhausted to atmosphere, the expanded supersonic jet is formed at a specific condition. In reality, the steam or moist air is usually used as working gas of supersonic moist air jet technologies. In these cases, non-equilibrium condensation may occur within the supersonic jet flow, and there are some researches on this phenomenon. On the other hand, in reality, there is a variety of engineering applications for discharge of the dry air into the atmosphere containing moist air or steam. In this case, non-equilibrium condensation may occur locally within the shear layer and affect the jet structure or energy loss in the flow field. However, the characteristics of non-equilibrium condensing flow in the jet shear layer are not investigated so far satisfactorily. The purpose of this study is to clarify the effect of local occurrence of non-equilibrium condensation in the shear layer on the characteristics of an under-expanded supersonic jet numerically. As a result, it was found that non-equilibrium condensation in shear layer affected the jet entrainment effect.

Keywords: Compressible flow, supersonic jet, non-equilibrium condensation, shear layer, simulation

Nomenclature

C_p	specific heat at constant pressure (J/kg·K)
D	diameter of nozzle exit (m)
D_m	diameter of Mach disk
$\boldsymbol{E}$, $\boldsymbol{F}$	numerical flux
g	condensate mass fraction
$\boldsymbol{H_1}$	source term of turbulence
$\boldsymbol{H_2}$	source term of axisymmetric
J	Jacobian
k	specific turbulence kinetic energy
L	distance from nozzle exit (m)
L_m	distance from nozzle exit to Mach disk

* Corresponding author. Tel.: +81-0952-28-8606; fax: +81-0952-28-8587.
E-mail address: matsuo@me.saga-u.ac.jp

M	Mach number
p	static pressure (Pa)
$\boldsymbol{Q}$	source term of condensation
$\boldsymbol{R}$, $\boldsymbol{S}$	Source term of vicosity
R	radius of wall curvature (m)
S	initial degree of supersaturation
$\boldsymbol{U}$	conservation mass term
$\boldsymbol{x}$, $\boldsymbol{y}$	Cartesian coordinate
Greek symbols	
ϕ	pressure ratio p/p_0
δ	boundary layer thicknesses(m)
μ	molecular viscosity (Pa·s)
ρ	density (kg/m^3)
τ	shear stress (Pa)
ω	specific dissipation rate
Subscripts	
0	stagnation point
1	vapor
2	dry air
t	turbulence

1. Introduction

When the high pressure gas is exhausted to atmosphere through the nozzle, the expanded supersonic jet is formed at a specific condition. The jet structure has been known as a fundamental phenomenon of the supersonic fluid mechanics. Supersonic jet has a great variety of engineering applications, such as supersonic aircrafts, jet propulsion thrust vectoring, fuel injectors for supersonic combustion, soot blower device, coating technology for structural materials and so on. Much effort has been devoted to study the characteristics of supersonic jets. According to these previous works, the supersonic jet is specified by its barrel shock structure, Mach disk location, jet boundary configuration, velocity decay, supersonic length and so on which are usually determined by the pressure ratio (Love, 1959, Mate, 2001). Especially, a lot of works have been done on the Mach disk structure, since it is important in determining the major characteristics of supersonic jets (Eastman, 1963, Addy, 1981).

In a variety of practical applications, the steam or moist air are usually used as working gas of supersonic moist air jet technologies such as power plants, industrial manufacturing processes and so on (Kim, 1996, Kim, 1996). In these cases, non-equilibrium condensation occurs within the supersonic jet flow, and there are some researches on this phenomenon. Karyshev, 1983 clarified that in order to estimate the rate of nucleation and condensate mass fraction in supersonic vapor jet, the latent heat of condensation has to be considered accurately. However, the structure of supersonic jet was not shown in this research. Recently, Beak et al., 2006 showed effects of relative humidity on under-expanded supersonic jet structures such as location and diameter of Mach disk and barrel shock wave experimentally. As a result, it was shown that the Mach disk diameter and location were strongly influenced by relative humidity of moist air. Otobe et al., 2006 investigated the effect of initial degrees of supersaturation on the characteristics of the axi-symmetric supersonic jet flow field numerically. As a result, it was found that the occurrence of the non-equilibrium condensation in the supersonic jet may reduce the noise level. Further, Otobe et al., 2009 investigated the hysteresis phenomenon of under-expanded dry and moist air jets, and it was clarified that the under-expanded moist air jet leads to less hysteresis of the jet compared with the dry air jets. In these researches, the non-equilibrium condensation occurred primarily within the supersonic jet flow.

On the other hand, in reality, there is a variety of engineering applications for discharge of the dry air into the atmosphere containing moisture or steam. In these cases, non-equilibrium condensation may occur locally within the shear layer and affect the jet structure or energy loss in the flow field. However, the flow characteristics with non - equilibrium in the jet shear layer are not investigated so far satisfactorily.

The purpose of this study is to clarify the effect of local occurrence of non-equilibrium condensation in the shear layer on the characteristics of an under-expanded supersonic jet numerically.

2. CFD Analysis

Like conventional two-phase flow analysis, several of assumptions were made for the present computations. There is no velocity slip and no temperature difference between condensate particles and medium gas flows, and due to very small condensate particles the effect of the particles on pressure field can be neglected within accuracy of present computations.

The governing equations, i.e., the unsteady two dimensional axisymmetric compressible Navier-Stokes equations combined with continuity, energy, nucleation rate, a droplet growth and diffusion equations (Bird et al., 1983, Hirschfelder, 1954) were written in

$$\frac{\partial \boldsymbol{U}}{\partial t}+\frac{\partial \boldsymbol{E}}{\partial \xi}+\frac{\partial \boldsymbol{F}}{\partial \eta}=\frac{1}{Re}\left(\frac{\partial \boldsymbol{R}}{\partial \xi}+\frac{\partial \boldsymbol{S}}{\partial \eta}\right)+\boldsymbol{H_1}+\boldsymbol{H_2}+\boldsymbol{Q} \tag{1}$$

where

$$\boldsymbol{U}=\frac{1}{J}\begin{bmatrix}\rho\\ \rho u\\ \rho v\\ E_t\\ \rho k\\ \rho\omega\\ \rho g\\ \rho D_1\\ \rho D_2\\ \rho D_3\\ \rho_1\end{bmatrix},\ \boldsymbol{E}=\frac{1}{J}\begin{bmatrix}\rho U\\ \rho uU+\xi_x p\\ \rho vU+\xi_y p\\ (E+p)U\\ \rho kU\\ \rho\omega U\\ \rho gU\\ \rho D_1U\\ \rho D_2U\\ \rho D_3U\\ \rho_1U\end{bmatrix},\ \boldsymbol{F}=\frac{1}{J}\begin{bmatrix}\rho V\\ \rho uV+\eta_x p\\ \rho vV+\eta_y p\\ (E+p)V\\ \rho kV\\ \rho\omega V\\ \rho gV\\ \rho D_1V\\ \rho D_2V\\ \rho D_3V\\ \rho_1V\end{bmatrix},\ \boldsymbol{R}=\frac{1}{J}\begin{bmatrix}0\\ \xi_x\tau_{xx}+\xi_y\tau_{xy}\\ \xi_x\tau_{xy}+\xi_y\tau_{yy}\\ \tau_{E,\xi}\\ f_k\left(\xi_x\frac{\partial k}{\partial x}+\xi_y\frac{\partial k}{\partial y}\right)\\ f_\omega\left(\xi_x\frac{\partial \omega}{\partial x}+\xi_y\frac{\partial \omega}{\partial y}\right)\\ 0\\ 0\\ 0\\ 0\\ \tau_{c1,\xi}\end{bmatrix},\ \boldsymbol{S}=\frac{1}{J}\begin{bmatrix}0\\ \eta_x\tau_{xx}+\eta_y\tau_{xy}\\ \eta_x\tau_{yx}+\eta_y\tau_{yy}\\ \tau_{E,\eta}\\ f_k\left(\eta_x\frac{\partial k}{\partial y}+\eta_y\frac{\partial k}{\partial y}\right)\\ f_\omega\left(\eta_x\frac{\partial \omega}{\partial y}+\eta_y\frac{\partial \omega}{\partial y}\right)\\ 0\\ 0\\ 0\\ 0\\ \tau_{c1,\eta}\end{bmatrix}$$

$$\boldsymbol{H_1}=\frac{1}{J}\begin{bmatrix}0\\ 0\\ 0\\ 0\\ P_k-\beta^*\rho\omega k\\ f_{\mathrm{H}}\\ 0\\ 0\\ 0\\ 0\\ 0\end{bmatrix},\ \boldsymbol{H_2}=\frac{1}{J}\begin{bmatrix}-\rho v\\ \tau_{xy}-\rho uv\\ \alpha-\rho v^2\\ \beta-(E_t+p)v\\ 0\\ 0\\ 0\\ 0\\ 0\\ 0\\ 0\end{bmatrix},\ \boldsymbol{Q}=\frac{1}{J}\begin{bmatrix}0\\ 0\\ 0\\ 0\\ 0\\ 0\\ \rho\dot{g}\\ \rho D_1\\ \rho D_2\\ \rho D_3\\ 0\end{bmatrix} \tag{2}$$

In Eq.(1), $\boldsymbol{U}$ is conservative vector, $\boldsymbol{E}$ and $\boldsymbol{F}$ are inviscid flux vector and $\boldsymbol{R}$ and $\boldsymbol{S}$ are viscous flux vectors. $\boldsymbol{H_1}$, $\boldsymbol{H_2}$ and $\boldsymbol{Q}$ are the source terms corresponding to turbulence, axisymmetric and condensation, respectively. $\boldsymbol{J}$ is Jacobian. τ_{xx}, τ_{xy}, τ_{yx} and τ_{yy} are components of viscous shear stress.

In Eq.(2),

$$\tau_{E,\xi}=\xi_x\left(q_x+u\tau_{xx}+v\tau_{xy}\right)+\xi_y\left(q_y+u\tau_{yx}+v\tau_{yy}\right),\ \tau_{E,\eta}=\eta_x\left(q_x+u\tau_{xx}+v\tau_{xy}\right)+\eta_y\left(q_y+u\tau_{yx}+v\tau_{yy}\right) \tag{3}$$

$$\tau_{c1,\xi}=\xi_x\left(\rho_1\Delta_1\frac{\partial c_1}{\partial x}\right)+\xi_y\left(\rho\Delta_1\frac{\partial c_1}{\partial y}\right),\ \tau_{c1,\eta}=\eta_x\left(\rho_1\Delta_1\frac{\partial c_1}{\partial x}\right)+\eta_y\left(\rho\Delta_1\frac{\partial c_1}{\partial y}\right) \tag{4}$$

$$q_{x_j}=\frac{1}{\gamma-1}\left(\frac{\mu}{Pr}+\frac{\mu_t}{Pr_{\mathrm{t}}}\right)\frac{\partial T}{\partial x_{\mathrm{j}}}+\rho\left(h_1\Delta_1\frac{\partial c_1}{\partial x_{\mathrm{j}}}+h_2\Delta_2\frac{\partial c_2}{\partial x_{\mathrm{j}}}\right) \tag{5}$$

$$f_k=\mu+\sigma*\frac{\rho k}{\omega},\ f_\omega=\mu+\sigma\frac{\rho k}{\omega},\ f_{\mathrm{H}}=\alpha\frac{\omega}{k}P_{\mathrm{k}}-\beta\rho\omega^2+\sigma_{\mathrm{d}}\frac{\rho}{\omega}\left(\frac{\partial k}{\partial x}\frac{\partial \omega}{\partial x}+\frac{\partial k}{\partial y}\frac{\partial \omega}{\partial y}\right) \tag{6}$$

$$P_{\mathrm{k}} = 2\mu_{\mathrm{t}}\left[\left(\frac{\partial u}{\partial x}\right)^2 + \frac{1}{2}\left(\frac{\partial v}{\partial x} + \frac{\partial u}{\partial y}\right) + \left(\frac{\partial v}{\partial y}\right)^2\right],\ \mu_{\mathrm{t}} = \frac{\rho k}{\tilde{\omega}}\ ,\ \tilde{\omega} = \max\left\{\sqrt{\frac{2\bar{S}_{\mathrm{i,j}}\bar{S}_{\mathrm{i,j}}}{\beta^*}}\right\} \tag{8}$$

$$\bar{S}_{\mathrm{i,j}} = S_{\mathrm{i,j}} - \frac{1}{3}\frac{\partial u_{\mathrm{k}}}{\partial x_{\mathrm{k}}},\ S_{\mathrm{i,j}} = \frac{1}{2}\left(\frac{\partial u_{\mathrm{i}}}{\partial x_{\mathrm{j}}} + \frac{\partial u_{\mathrm{j}}}{\partial x_{\mathrm{i}}}\right) \tag{9}$$

$$\alpha = \frac{1}{Re}\left(\tau_{yy} - \tau_{tt}\right),\ \beta = \frac{1}{Re}\left\{u\tau_{\mathrm{xx}} - v\tau_{\mathrm{yy}} + \frac{\left(\mu + \mu_{\mathrm{t}}\right)\partial T}{Pr\left(\gamma\text{-}1\right)\partial y}\right\},\ \tau_{\mathrm{tt}} = -\frac{2}{3}\mu\left(\frac{\partial u}{\partial x} + \frac{\partial v}{\partial y} - 2\frac{v}{y}\right) \tag{10}$$

The density of gas mixture is calculated by the sum of density of vapor (ρ_1) and dry air (ρ_2) ;

$$\rho = \rho_1 + \rho_2 \tag{12}$$

The mass fraction can be given as

$$c_{\mathrm{i}} = \frac{\rho_{\mathrm{i}}}{\rho} \tag{13}$$

In equations (4) and (5) Δ_1 and Δ_2 are effective diffusivities. The closure coefficients are,

$$\beta = 0.0708,\ \alpha = \frac{13}{25},\ \beta^* = \frac{9}{100},\ \sigma = \frac{1}{2},\ \sigma^* = \frac{3}{5},\ Pr_{\mathrm{t}} = \frac{7}{8} \tag{14}$$

$$\sigma_{\mathrm{d}} = \begin{cases} 0, & \dfrac{\partial k}{\partial x_{\mathrm{j}}}\dfrac{\partial \omega}{\partial x_{\mathrm{j}}} \le 0 \\ \sigma_{\mathrm{d0}}, & \dfrac{\partial k}{\partial x_{\mathrm{j}}}\dfrac{\partial \omega}{\partial x_{\mathrm{j}}} \ge 0 \quad \left(\sigma_{\mathrm{d0}} = \dfrac{1}{8}\right) \end{cases} \tag{15}$$

The governing equation systems that are non-dimensionalized with reference values at the reservoir condition were mapped from the physical plane into a computational plane of general transform. To close the governing equations, *k*-ω model (Wilcox, 2008) was employed in computations. A third-order TVD finite difference scheme with MUSCL (Yee, 1989) was used to discretize the spatial derivatives, and second-order central difference scheme for the viscous term, and a second-order fractional step method (Strang, 1976) was employed for time integration.

3. Computational Conditions

Figure 1 shows the schematics of computational domain of the flow field and boundary conditions. The height of nozzle exit D is 12.7 mm. The radius of curvature R is 12.7 mm.

Table 1 shows the initial conditions used in the present simulation. Back pressure (stagnation pressure downstream of the nozzle) p_{b} is 101.3 kPa. Total pressure of stagnation point upstream of the nozzle are $3.8p_{\mathrm{b}}$ (Cases 1 and 2) and $6.2p_{\mathrm{b}}$ (Cases 3 and 4). Total temperature of stagnation point upstream of the nozzle is 298 K. Dry air upstream of the nozzle was discharged to the atmosphere containing dry air or moist air downstream of the nozzle exit. Initial degrees of supersaturation at the stagnation point downstream of the nozzle are $S_{0\mathrm{b}}$=0.0 (Cases 1 and 3) and $S_{0\mathrm{b}}$=0.7 (Cases 2 and 4).

The adiabatic no-slip wall condition was used on solid wall as boundary condition. The boundary conditions at inlet and exit were set at fixed condition and outflow condition, respectively. Condensate mass fraction g was set at g=0 on the solid wall.

4. Result and discussions

Figure 2 shows comparison of Mach disk diameter D_{m} and the distance L_{m} from nozzle exit to Mach disk between simulated and experimental results (Otobe, et al., 2006). As seen from this figure, the present simulations with the number of

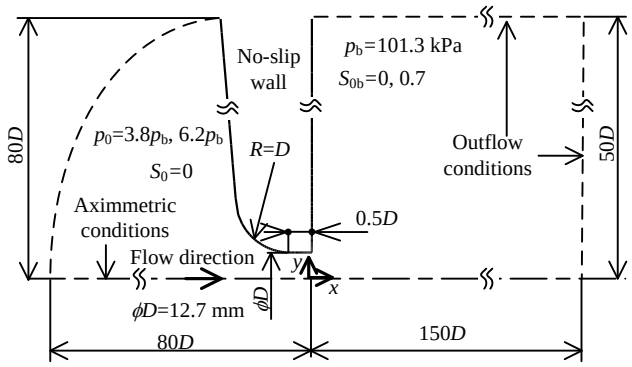

Fig. 1. Computational domain and boundary conditions

Table 1. Initial conditions

	ϕ	S_{0b}	p_0	T_0[K]
Case 1	3.8	0	101.3	298
Case 2		0.7		
Case 3	6.2	0		
Case 4		0.7		

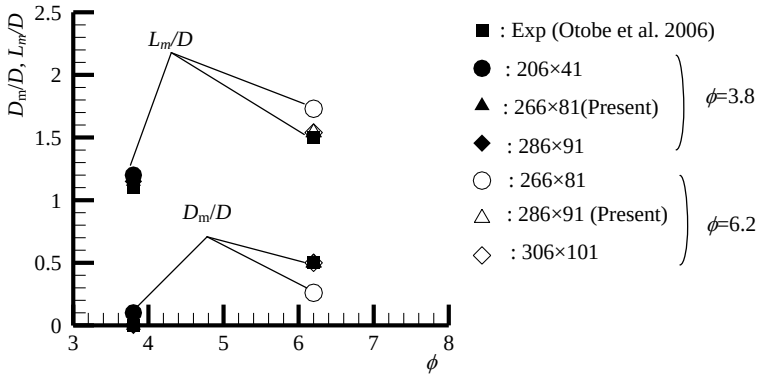

Fig. 2. Comparison between experimental and simulated results.

grids of 266×81 and 286×91 for ϕ=3.8, and 286×91 and 306×101 for ϕ=6.2 are good agreement with experimental results. In this study, 266×81 for ϕ=3.8 and 286×91 for ϕ=6.2 were used in order to prevent the consumption of computation time.

In order to show the validity of the simulation, some experiments were conducted. In experiments, total pressure and total temperature at stagnation point upstream of the nozzle are 101.3 kPa and 298 K, respectively. Initial degrees of supersaturation of stagnation point upstream of the nozzle are S_{0b}=0.0 and S_{0b}=0.7. The initial degree of supersaturation of back pressure downstream of the nozzle exit is S_{0b}=0.0 (dry air). Figures 3(a), (b), (c) and (d) show comparison between the experimental and simulated results. For each figure, figures of the upper and lower sides are time-averaged contour maps of static pressure obtained by simulation and schlieren photographs in experiments, respectively. As seen from these figures, simulated results are good agreement with experimental ones.

Figures 4(a), (b), (c) and (d) show time-averaged contour maps of Mach number (solid lines) and condensate mass fraction for Cases 1 to 4, respectively. For ϕ=3.8 (Figs. 4(a) and 4(b)), regular reflection is observed in the flow field. In the case of ϕ=6.2(Figs. 4(c) and 3(d)), Mach reflection is observed. In cases of Figs. 4(b) and 4(d), condensate droplets expand over shear layer. As seen from these figure, values of condensate mass fraction for Fig. 4(d) (ϕ=6.2) is larger than Fig. 4(b) (ϕ=3.8).

Figures 5(a) and (b) show time-averaged contour maps of static pressure (solid line), nucleation rate (red) and stream line (line with arrow). As seen from these figures, stream line of the flow is toward the jet. As is evident from these figures, the presence of condensate nuclei in the shear layer is confirmed and they are generated from x/D=0.5 for ϕ=3.8 and x/D=0.1 for ϕ=6.2.

Figures 6(a) and (b) show distributions of mass fluxes along the vertical lines at x/D=1.0, 2.0 and 3.0 for all cases. The abscissa is the mass fluxes $\rho u/\rho_0 a_0$ and the ordinate is distance from nozzle axis y/D. As seen from these figure, the mass fluxes for Cases 2 and 4 are large in subsonic region and small in supersonic region of shear layer in comparison with Cases 1 and 3. This is due to release of latent heat by occurrence of non-equilibrium condensation in shear layer. Difference of mass flux becomes large with an increase of distance from nozzle exit.

Figures 7(a) and (b) show time-averaged distributions of the mass flow rate in the jet region for all cases. The abscissa is distance x/D from nozzle exit, and the mass flow rate ρuA which normalized by the mass flow rate at nozzle exit $(\rho uA)_{\text{exit}}$ is on the ordinate. As is evident from these figures, mass flow rate of Case 2 increases compared with that of Case 1. However, for Case 4, mass flow rate decreases in comparison with that of Case 3. This means that non - equilibrium condensation in the shear layer induces the change of jet entrainment effect.

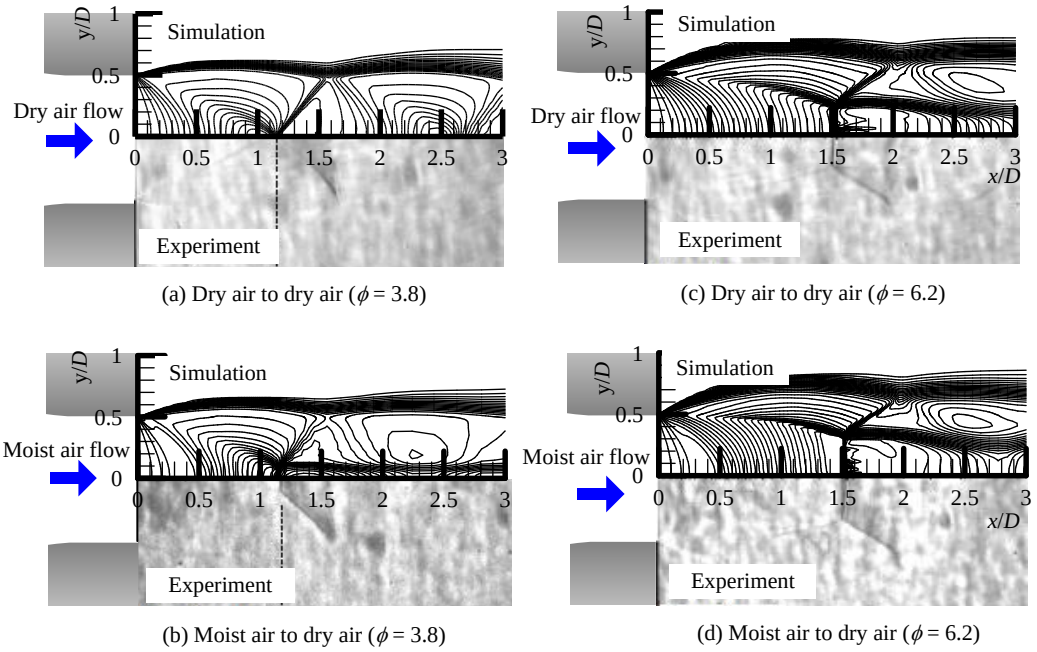

Fig. 3. Comparison between experimental and simulated results.

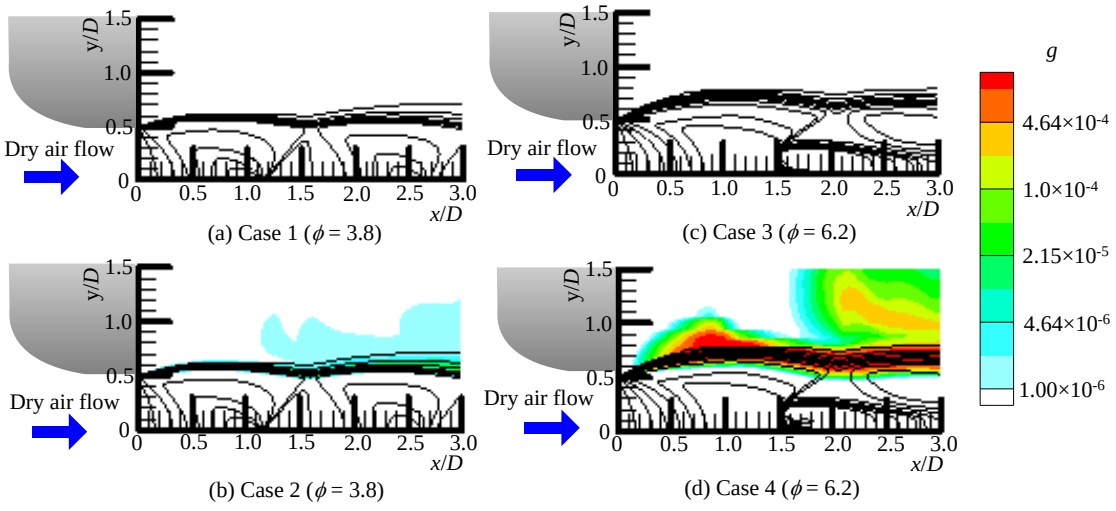

Fig. 4. Time-averaged contour maps of Mach number M (solid line) and condensate mass fraction g (color)

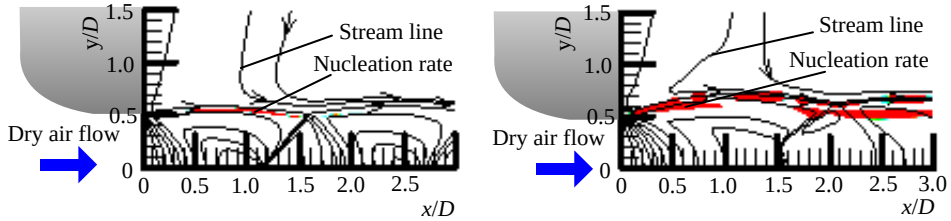

(a) Case 2 (ϕ = 3.8) (b) Case 4 (ϕ = 6.2)

Fig. 5. Time-averaged contour maps of Static pressure p/p_0 (solid line), nucleation rate I (red) and stream line (line with arrow).

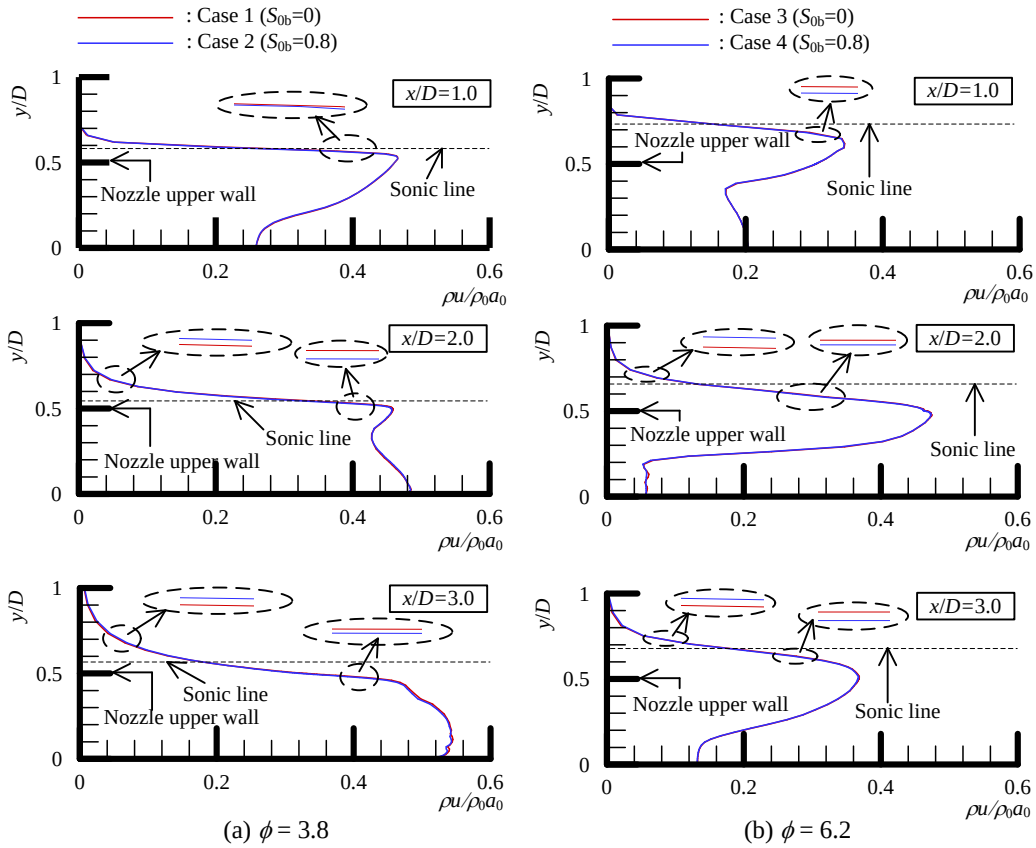

(a) ϕ = 3.8 (b) ϕ = 6.2

Fig. 6. Time-averaged distributions of mass fluxes $\rho u/\rho_0 a_0$

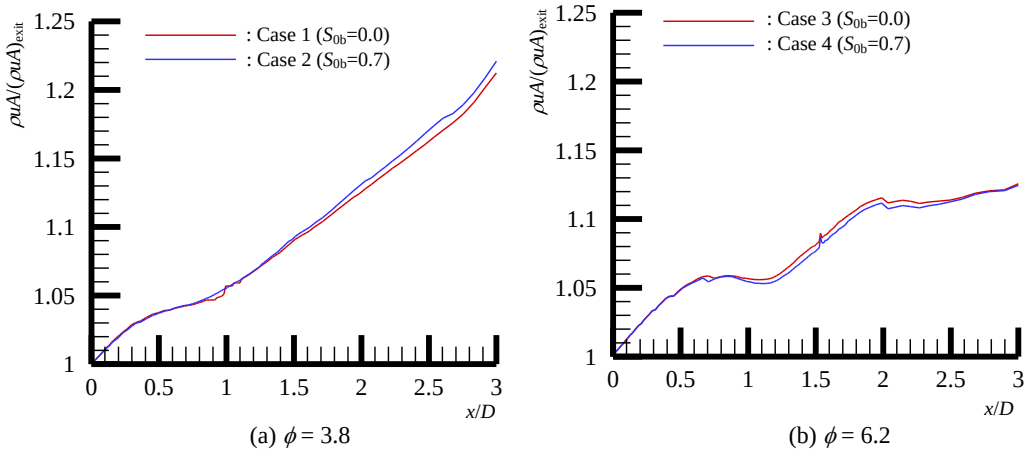

(a) ϕ = 3.8 (b) ϕ = 6.2

Fig. 7. Time-averaged distributions of mass flow rate $\rho uA/(\rho uA)_{exit}$

5. Conclusions

A numerical study has been made to investigate the effect of non-equilibrium condensation occurred in the shear layer on characteristics of an under-expanded supersonic jet. The results obtained are summarized as follows:

(1) Simulated results were a good agreement with experimental data.
(2) In the case of dry air discharged to an atmosphere with moisture, non-equilibrium condensation occurred in shear layer of supersonic jet.
(3) In the case of dry air discharged to an atmosphere with moisture, mass fluxes decreased with an increase of distance from nozzle exit.
(4) Non-equilibrium condensation occurred in shear layer affected jet entrainment.

References

[1] Love E.S., Grigsby D.E., Lee L.P., 1959. Experimental and Theoretical Studies of Axisymmetric Free Jets, NASA TR R-6.
[2] Mate B., Graur I.A., Elizarova T., Chirokov I., Tejeda G., Femandez J.M., Montero S., 2001. Experimental and Numerical Investigation of an Axisymmetric Supersonic Jet., Journal of Fluids Mechanics, Vol. 426, p. 177-197.
[3] Eastman D.W., Radtke L.P., 1963. Location of the Normal Shock Wave in the Exhaust Plume of a Jet, AIAA Journal., Vol. 11, No. 4, p. 918-919
[4] Addy A.L., 1981. Effect of Axisymmetric Sonic Nozzle Geometry on Mach Disk Characteristics, AIAA Journal, Vol.19, No. 1, pp.121-122.
[5] Kim H.D., Shin H.S., 1996. Numerical Study on Under-Expanded Jets through a Supersonic Nozzle(Part 2), Journal of Korea Society of Mechanical Engineers. Series(B)., Vol. 20, NO.6, p. 1994-2004.
[6] Kim H.D., Lee J.S., 1996, An Experimental Study on Supersonic Jet Issuing from Gas Atomizing Nozzle(Part 1), Journal of Korea Society of Mechanical Engineers. Series (b), Vol. 20, No. 2, p. 677-709.
[7] Karyshey A.K., 1983. Experimental Study of the Turbulent Boundary Layer of a Jet with Condensation., Fluid Dynamics-Soviet Research., Vol. 12, No. 1, p. 87-91.
[8] Beak S.C., Kwon S.B, Kim H.D., Setoguchi T., Matsuo S., 2006. A Study of Moderately Under-Expanded Supersonic Moist Air Jets, AIAA Journal, Vol. 44, No.7, p. 1624-1627.
[9] Otobe Y., Matsuo S., Tanaka T., Kashimura H., Setoguchi T., 2006. A Study on Characteristics of Under-Expanded Condensing Jet, Journal of Science and Technology. Series B, Vol. 149, No. 4, p. 1165-1172.
[10] Otobe Y., Yasunobu T., Kashimura H., Matsuo S., Setoguchi T., Kim H.D., 2009. Hysterisis Phenomenon of Underexpanded Moist Air Jet, AIAA Journal, Vol. 47, No. 12, p. 2792-2799.
[11] Bird R.B, Stewart W.E, Lightfoot E.N., 1960. Transport Phenomena, Wiley, New York.
[12] Hirschfelder J.O, Curtiss C.F, Bird R.B., 1954. Molecular Theory of Gases and Liquids, Wiley, New York.
[13] Wilcox D.C., 2008. Formulation of the *k*-ω Turbulence Model Revisited, AIAA Journal, Vol. 46, No. 11, p. 282-2838.
[14] Yee, H.C., A Class of High-resolution explicit and implicit shock capturing methods, NASA-TM-89464.
[15] Strang G., 1976. Linear Algebra and Its Applications, Massachusetts Institute of Technology.

Available online at www.sciencedirect.com

SciVerse ScienceDirect

Procedia Engineering 00 (2012) 000–000

Procedia Engineering

www.elsevier.com/locate/procedia

5th BSME International Conference on Thermal Engineering

Effect of non-equilibrium condensation in shear layer on supersonic impinging jets

Shigeru Matsuo[a]*, Mamun Mohammad[b], Junji Nagao[c], Tokitada Hashimoto[a], Toshiaki Setoguchi[d] and Heuy Dong Kim[e]

[a]*Department of Advanced Technology Fusion, Saga University, 1 Honjo-machi, Saga 840-8502, Japan*
[b]*Department of Mechanical Engineering, Bangladesh University of Engineering & Technology, Dhaka 1000, Bangladesh*
[c]*Graduate School of Science & Engineering, Saga University, 1 Honjo-machi, Saga-shi, Saga 840-8502, Japan*
[d]*Institute of Ocean Energy, Saga University, 1 Honjo-machi, Saga-shi, Saga 840-8502, Japan*
[e]*School of Mechanical Engineering, Andong National University, 388 Song Cheon Dong, Andong 760-749, Korea*

Abstract

Impinging jet on a solid surface can be found in various engineering applications. In the flow fields, the characteristics of impinging jet are generally found to become complex extremely. In various industrial jet technologies such as jet burner, steam turbine and so on, condensable gas is often used as working gas. In these cases, the non-equilibrium condensation may occur at the region between nozzle exit and an object. On the other hand, in reality, there is a variety of engineering applications for discharge of the dry air into the atmosphere with moisture. In this case, non-equilibrium condensation may occur in the shear layer and affect the jet structure or energy loss in the flow field. However, the feature of non-equilibrium condensing flow in the jet shear layer are not investigated so far satisfactorily. In the present study, the effect of local occurrence of non-equilibrium condensation in shear layer on the characteristics of an under-expanded supersonic impinging jet was investigated numerically. As a result, non-equilibrium condensation occurred in shear layer and increased the displacement thickness on flat plate.

Keywords: Compressible flow, supersonic inpinjing jet, non-equilibrium condensation, shear layer, simulation

Nomenclature

C_p	specific heat at constant pressure (J/kg·K)
D	diameter of nozzle exit (m)
$\boldsymbol{E}$, $\boldsymbol{F}$	numerical flux
g	condensate mass fraction
$\boldsymbol{H}_1$	source term of turbulence
$\boldsymbol{H}_2$	source term of axisymmetric
J	Jacobian
k	specific turbulence kinetic energy
L	distance from nozzle exit (m)
M	Mach number

* Corresponding author. Tel.: +81-0952-28-8606; fax: +81-0952-28-8587.
E-mail address: matsuo@me.saga-u.ac.jp

p	static pressure (Pa)
$\boldsymbol{Q}$	source term of condensation
$\boldsymbol{R}$, $\boldsymbol{S}$	Source term of viscosity
R	radius of wall curvature (m)
S	initial degree of supersaturation
$\boldsymbol{U}$	conservation mass term
$\boldsymbol{x}$, $\boldsymbol{y}$	Cartesian coordinate
Greek symbols	
δ^*	displacement thickness (m)
ϕ	pressure ratio p/p_0
μ	molecular viscosity (Pa·s)
ρ	density (kg/m^3)
τ	shear stress (Pa)
ω	specific dissipation rate
Subscripts	
0	stagnation point
1	vapor
2	dry air
t	turbulence

1. Introduction

Impinging jet on a solid surface can be found in various engineering applications, such as the landing or take-off of a V/STOL aircraft, impingement of a jet engine exhaust, terrestrial rocket launch, laser cutting in the manufacturing industries, thrust control system of a solid rocket motor and so on (Lamont et al., 1980, Kalghatgi et al., 1976, Masuda et al., 1994).

These impinging jet flow fields are generally found to be extremely complex. The supersonic jet impinging vertically on a flat plate is known as the flow that contains the mixed regions of subsonic and supersonic flows, interaction between shock and expansion waves, turbulent shear flow region, and self-induced shock oscillation. The structure of impinging jet is dependent on the design Mach number, that is, nozzle geometry, nozzle pressure ratio, the distance between nozzle exit and flat plate and so on.

On the other hand, in the supersonic flow of an actual jet burner, a steam turbine cascade and various industrial jet technologies, condensable gas is used as working gas. In these cases, the non-equilibrium condensation (Wegener, 1958, Matsuo, 1985) may occur at the region between nozzle exit and an object. In the past study, in the case with non-equilibrium condensation occurred in the supersonic jet, frequency of oscillation for the flow field becomes larger than that without the non-equilibrium condensation, and amplitudes of static pressure become small compared with those of dry air. Furthermore, in reality, there is a variety of engineering applications for discharge of the dry air into the atmosphere with moisture. In this case, non-equilibrium condensation may occur in the shear layer and affect the jet structure or energy loss in the flow field. However, the flow characteristics with non-equilibrium condensation in the jet shear layer are not investigated so far satisfactorily.

In the present study, the effect of local occurrence of non-equilibrium condensation in shear layer on the characteristics of an under-expanded supersonic impinging jet was investigated numerically.

2. CFD Analysis

Like conventional two-phase flow analysis, several of assumptions were made for the present computations. There is no velocity slip and no temperature difference between condensate particles and medium gas flows, and due to very small condensate particles the effect of the particles on pressure field can be neglected within accuracy of present computations.

The governing equations, i.e., the unsteady two dimensional axisymmetric compressible Navier-Stokes equations combined with continuity, energy, nucleation rate, a droplet growth and diffusion equations (Bird et al., 1983, Hirschfelder, 1954) were written in

$$\frac{\partial \boldsymbol{U}}{\partial t}+\frac{\partial \boldsymbol{E}}{\partial \xi}+\frac{\partial \boldsymbol{F}}{\partial \eta}=\frac{1}{Re}\left(\frac{\partial \boldsymbol{R}}{\partial \xi}+\frac{\partial \boldsymbol{S}}{\partial \eta}\right)+\boldsymbol{H_1}+\boldsymbol{H_2}+\boldsymbol{Q} \tag{1}$$

where

$$\boldsymbol{U}=\frac{1}{J}\begin{bmatrix}\rho\\ \rho u\\ \rho v\\ E_t\\ \rho k\\ \rho\omega\\ \rho g\\ \rho D_1\\ \rho D_2\\ \rho D_3\\ \rho_1\end{bmatrix},\ \boldsymbol{E}=\frac{1}{J}\begin{bmatrix}\rho U\\ \rho uU+\xi_x p\\ \rho vU+\xi_y p\\ (E+p)U\\ \rho kU\\ \rho\omega U\\ \rho gU\\ \rho D_1U\\ \rho D_2U\\ \rho D_3U\\ \rho_1U\end{bmatrix},\ \boldsymbol{F}=\frac{1}{J}\begin{bmatrix}\rho V\\ \rho uV+\eta_x p\\ \rho vV+\eta_y p\\ (E+p)V\\ \rho kV\\ \rho\omega V\\ \rho gV\\ \rho D_1V\\ \rho D_2V\\ \rho D_3V\\ \rho_1V\end{bmatrix},\ \boldsymbol{R}=\frac{1}{J}\begin{bmatrix}0\\ \xi_x\tau_{xx}+\xi_y\tau_{xy}\\ \xi_x\tau_{xy}+\xi_y\tau_{yy}\\ \tau_{E,\xi}\\ f_k\left(\xi_x\frac{\partial k}{\partial x}+\xi_y\frac{\partial k}{\partial y}\right)\\ f_\omega\left(\xi_x\frac{\partial \omega}{\partial x}+\xi_y\frac{\partial \omega}{\partial y}\right)\\ 0\\ 0\\ 0\\ 0\\ \tau_{c1,\xi}\end{bmatrix},\ \boldsymbol{S}=\frac{1}{J}\begin{bmatrix}0\\ \eta_x\tau_{xx}+\eta_y\tau_{xy}\\ \eta_x\tau_{yx}+\eta_y\tau_{yy}\\ \tau_{E,\eta}\\ f_k\left(\eta_x\frac{\partial k}{\partial y}+\eta_y\frac{\partial k}{\partial y}\right)\\ f_\omega\left(\eta_x\frac{\partial \omega}{\partial y}+\eta_y\frac{\partial \omega}{\partial y}\right)\\ 0\\ 0\\ 0\\ 0\\ \tau_{c1,\eta}\end{bmatrix}$$

$$\boldsymbol{H_1}=\frac{1}{J}\begin{bmatrix}0\\ 0\\ 0\\ 0\\ P_k-\beta^*\rho\omega k\\ f_{\mathrm{H}}\\ 0\\ 0\\ 0\\ 0\\ 0\end{bmatrix},\ \boldsymbol{H_2}=\frac{1}{J}\begin{bmatrix}-\rho v\\ \tau_{xy}-\rho uv\\ \alpha-\rho v^2\\ \beta-(E_t+p)v\\ 0\\ 0\\ 0\\ 0\\ 0\\ 0\\ 0\end{bmatrix},\ \boldsymbol{Q}=\frac{1}{J}\begin{bmatrix}0\\ 0\\ 0\\ 0\\ 0\\ 0\\ \rho\dot{g}\\ \rho D_1\\ \rho D_2\\ \rho D_3\\ 0\end{bmatrix} \tag{2}$$

In Eq.(1), $\boldsymbol{U}$ is conservative vector, $\boldsymbol{E}$ and $\boldsymbol{F}$ are inviscid flux vector and $\boldsymbol{R}$ and $\boldsymbol{S}$ are viscous flux vectors. $\boldsymbol{H_1}$, $\boldsymbol{H_2}$ and $\boldsymbol{Q}$ are the source terms corresponding to turbulence, axisymmetric and condensation, respectively. $\boldsymbol{J}$ is Jacobian. τ_{xx}, τ_{xy}, τ_{yx} and τ_{yy} are components of viscous shear stress.

In Eq.(2),

$$\tau_{E,\xi}=\xi_x\left(q_x+u\tau_{xx}+v\tau_{xy}\right)+\xi_y\left(q_y+u\tau_{yx}+v\tau_{yy}\right),\quad \tau_{E,\eta}=\eta_x\left(q_x+u\tau_{xx}+v\tau_{xy}\right)+\eta_y\left(q_y+u\tau_{yx}+v\tau_{yy}\right) \tag{3}$$

$$\tau_{c1,\xi}=\xi_x\left(\rho_1\Delta_1\frac{\partial c_1}{\partial x}\right)+\xi_y\left(\rho\Delta_1\frac{\partial c_1}{\partial y}\right),\ \tau_{c1,\eta}=\eta_x\left(\rho_1\Delta_1\frac{\partial c_1}{\partial x}\right)+\eta_y\left(\rho\Delta_1\frac{\partial c_1}{\partial y}\right) \tag{4}$$

$$q_{x_j}=\frac{1}{\gamma-1}\left(\frac{\mu}{Pr}+\frac{\mu_t}{Pr_{\mathrm{t}}}\right)\frac{\partial T}{\partial x_{\mathrm{j}}}+\rho\left(h_1\Delta_1\frac{\partial c_1}{\partial x_{\mathrm{j}}}+h_2\Delta_2\frac{\partial c_2}{\partial x_{\mathrm{j}}}\right),\ f_{\mathrm{k}}=\mu+\sigma*\frac{\rho k}{\omega},\ f_{\omega}=\mu+\sigma\frac{\rho k}{\omega}, \tag{5}$$

$$f_{\mathrm{H}}=\alpha\frac{\omega}{k}P_{\mathrm{k}}-\beta_{\mathrm{a}}\rho\omega^2+\sigma_{\mathrm{d}}\frac{\rho}{\omega}\left(\frac{\partial k}{\partial x}\frac{\partial \omega}{\partial x}+\frac{\partial k}{\partial y}\frac{\partial \omega}{\partial y}\right),\ P_{\mathrm{k}}=2\mu_{\mathrm{t}}\left[\left(\frac{\partial u}{\partial x}\right)^2+\frac{1}{2}\left(\frac{\partial v}{\partial x}+\frac{\partial u}{\partial y}\right)+\left(\frac{\partial v}{\partial y}\right)^2\right] \tag{6}$$

$$\mu_{\mathrm{t}}=\frac{\rho k}{\tilde{\omega}},\ \tilde{\omega}=\max\left\{\sqrt{\frac{2\bar{S}_{\mathrm{i,j}}\bar{S}_{\mathrm{i,j}}}{\beta*}}\right\},\ \bar{S}_{\mathrm{i,j}}=S_{\mathrm{i,j}}-\frac{1}{3}\frac{\partial u_{\mathrm{k}}}{\partial x_{\mathrm{k}}},\ S_{\mathrm{i,j}}=\frac{1}{2}\left(\frac{\partial u_{\mathrm{i}}}{\partial x_{\mathrm{j}}}+\frac{\partial u_{\mathrm{j}}}{\partial x_{\mathrm{i}}}\right) \tag{7}$$

$$\alpha=\frac{1}{Re}\left(\tau_{yy}-\tau_{tt}\right),\ \tau_{\mathrm{tt}}=-\frac{2}{3}\mu\left(\frac{\partial u}{\partial x}+\frac{\partial v}{\partial y}-2\frac{v}{y}\right) \tag{8}$$

The density of gas mixture is calculated by the sum of density of vapor (ρ_1) and dry air (ρ_2) ；

$$\rho = \rho_1 + \rho_2 \tag{9}$$

The mass fraction can be given as

$$c_{\mathrm{i}} = \frac{\rho_{\mathrm{i}}}{\rho} \tag{10}$$

In equations (4) and (5) Δ_1 and Δ_2 are effective diffusivities. The closure coefficients are,

$$\beta_{\mathrm{a}} = 0.0708,\ \alpha = \frac{13}{25},\ \beta^* = \frac{9}{100},\ \sigma = \frac{1}{2},\ \sigma^* = \frac{3}{5},\ Pr_{\mathrm{t}} = \frac{7}{8} \tag{11}$$

$$\sigma_{\mathrm{d}} = \begin{cases} 0, & \dfrac{\partial k}{\partial x_{\mathrm{j}}}\dfrac{\partial \omega}{\partial x_{\mathrm{j}}} \le 0 \\ \sigma_{\mathrm{d0}}, & \dfrac{\partial k}{\partial x_{\mathrm{j}}}\dfrac{\partial \omega}{\partial x_{\mathrm{j}}} \ge 0 \quad \left(\sigma_{\mathrm{d0}} = \dfrac{1}{8}\right) \end{cases} \tag{12}$$

The governing equation systems that are non-dimensionalized with reference values at the reservoir condition were mapped from the physical plane into a computational plane of general transform. To close the governing equations, k-ω model (Wilcox, 2008) was employed in computations. A third-order TVD finite difference scheme with MUSCL (Yee, 1989) was used to discretize the spatial derivatives, and second-order central difference scheme for the viscous term, and a second-order fractional step method (Strang, 1976) was employed for time integration.

3. Computational Conditions

Figure 1 shows a schematic diagram of computational domain of the flow field and boundary conditions. The height of nozzle exit D is 12.7 mm. The radius of curvature R is 12.7 mm. The distance from nozzle exit to flat plate L/D=2.3. A time histories of static pressure was measured at point A in Fig. 1.

Table 1 shows the computational conditions used in present calculation. Back pressure (stagnation pressure downstream of the nozzle) p_{b0} is 101.3 kPa. Values of total pressure of stagnation point upstream of the nozzle are $3.0p_{\mathrm{b}}$ (Cases1 and 2) and $6.2p_{\mathrm{b}}$ (Cases 3 and 4). Total temperature of stagnation point upstream of the nozzle is 293 K. Dry air upstream of the nozzle was discharged to the atmosphere of dry air or with moisture downstream of the nozzle exit. Initial degrees of supersaturation at the stagnation point downstream of the nozzle are $S_{0\mathrm{b}}$=0 (Cases 1 and 3) and $S_{0\mathrm{b}}$=0.8 (Cases 2 and 4).

The adiabatic no-slip wall condition was used on solid wall as boundary condition. The boundary conditions at inlet and exit were set at fixed condition and outflow condition, respectively. Condensate mass fraction g was set at g=0 on the solid wall.

4. Result and discussions

Table 2 shows comparison of the dominant frequency between the simulated and experimental results (Sakakibara et al., 1998). The pressure ratio ϕ is 3.0. As seen from this table, the dominant frequencies obtained by the present simulation with the number of grids of 254×81 and 274×91 are good agreement with experimental result. In this study, 254×81 was used in order to prevent the consumption of computation time.

Figures 2(a) and (b) show time-averaged contour maps of Mach number for ϕ = 3.0 and ϕ = 6.2, respectively. The initial degrees of supersaturation at stagnation point downstream of the nozzle exit are $S_{0\mathrm{b}}$=0 (dry air) and $S_{0\mathrm{b}}$=0.8 (moist air). In the case of ϕ = 3.0(Fig. 2(a)), a plate shock exists at x/D=2.0. For ϕ=6.2, the plate shock is observed at x/D=1.5. From these figures, the difference for Mach number contour is not observed obviously.

Figure 3 show time-averaged contour maps of condensate mass fraction for Case 2(ϕ = 3.0) and Case 3(ϕ = 6.2). Initial degree of supersaturation at stagnation downstream of the nozzle exit is $S_{0\mathrm{b}}$=0.8. In the case of Case 4(ϕ=6.2), the condensate mass fraction g begins to increase rapidly in the shear layer of the jet and condensate droplets are generated in

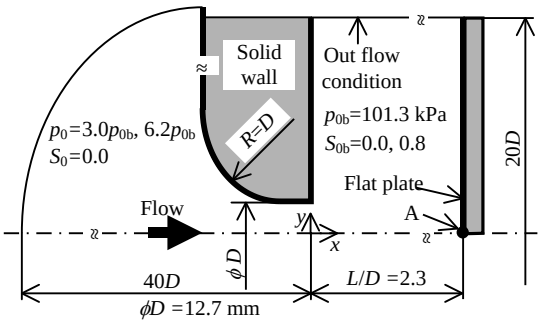

Fig. 1.Computational domain and boundary conditions

Table 1 Computational conditions

	ϕ	S_{0b}	p_{0b} [kPa]	T_0 [K]
Case 1	3.0	0	101.3	293
Case 2		0.8		
Case 3	6.2	0		
Case 4		0.8		

Table 2 Comparison with present simulation and experiment

		ϕ= 3.0
	Mesh number	Frequency (kHz)
Simulation	274×91	24.7
	254×81 (Present)	24.7
	114×36	20.5
Experiment (Sakakibara et al., 1998)	-	25.3

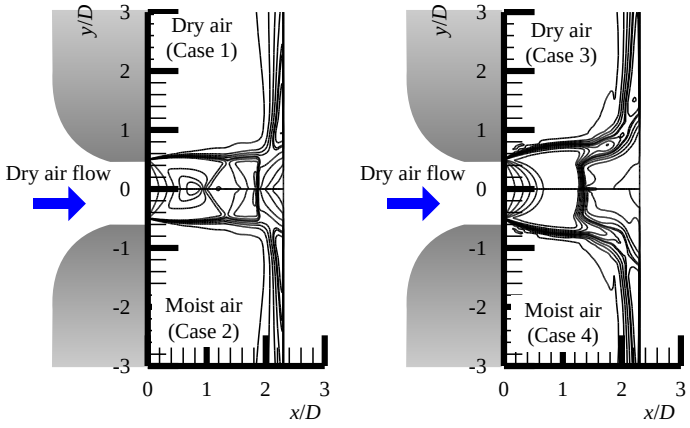

Fig. 2 Time-averaged contour maps of Mach number *M*

the shear layer of the jet. This is due to the rapidly expansion of moist air entrained by supersonic jet downstream of the nozzle exit. In the case of ϕ=3.0, condensate droplets are not observed in shear layer.

Figures 4(a) and (b) show time-averaged static pressure distributions on flat plate for ϕ=3.0 and ϕ=6.2, respectively. The initial degrees of supersaturation at stagnation point downstream of the nozzle exit are S_{0b}=0(red line) and S_{0b}=0.8 (blue line). The abscissa is the static pressure p divided by stagnation pressure upstream of the nozzle p_0 and the ordinate is distance from nozzle center line y/D. In the case of Fig. 4(b), static pressure of moist air (Case 4) is small in comparison with that of

dry air. This is due to increase of Mach number by non-equilibrium condensation in shear layer (subsonic region). However, in Fig. 4(a), the difference of static pressure p/p_0 on the wall between the dry air and moist air at stagnation point downstream of the nozzle exit was not observed.

Figures 5(a) and (b) show the time-averaged distributions of Mach number along y - axis at x/D=0.5, 1.8 (Cases 1 and 2) and 1.1 (Cases 3 and 4) for ϕ=3.0 and ϕ=6.2, respectively. Initial degrees of supersaturation at stagnation point downstream of the nozzle exit are S_{0b}=0 (red line) and S_{0b}=0.8 (blue line). As seen from these figures, Mach number for Case 4 (S_{0b}=0.8)

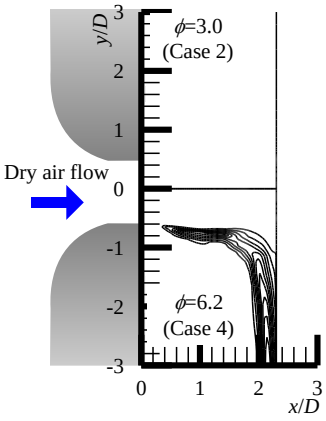

Fig. 3 Time-averaged contour maps of condensate mass fraction g

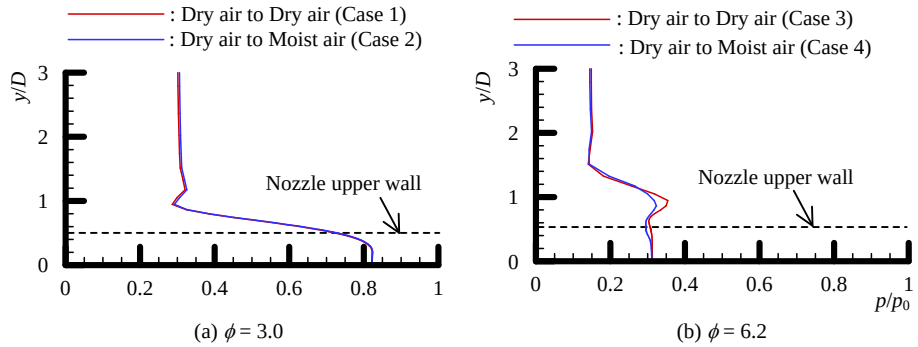

Fig. 4 Time-averaged distributions of static pressure on the flat plate p/p_0

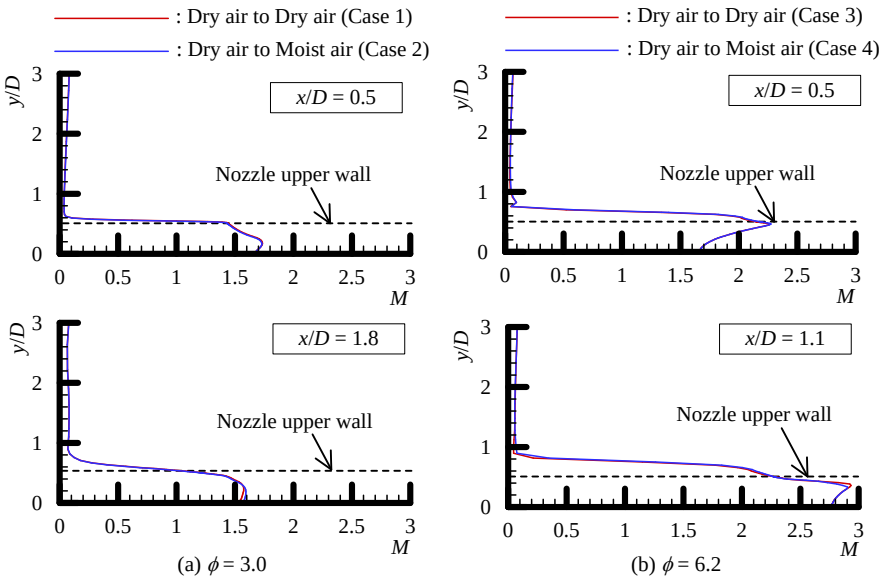

Fig. 5 Time-averaged distributions of Mach number M

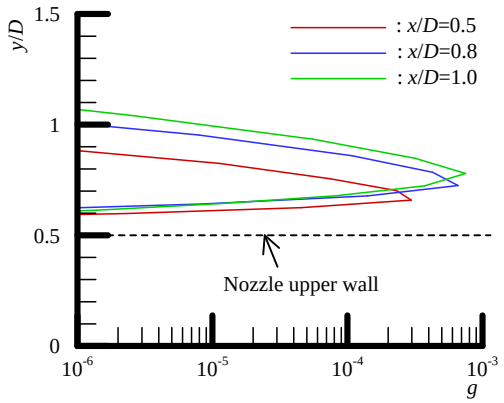

Fig. 6 Time-averaged distributions of condensate mass fraction g (Case 4)

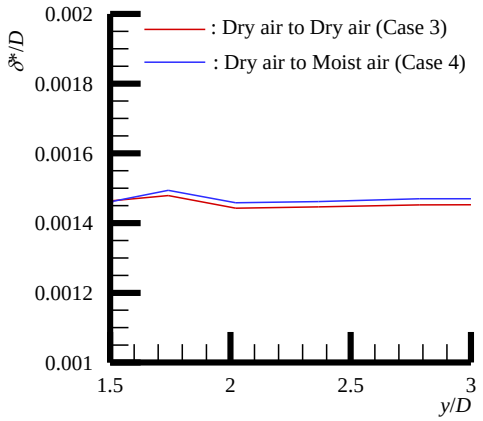

Fig. 7 Time-averaged distributions of displacement thickness δ^*/D on flat plate (ϕ=6.2)

is small compared with that of Case 3 (S_{0b}=0). It is considered that this is due to the release of latent heat by non-equilibrium condensation in the shear layer.

Figure 6 shows time-averaged distributions of condensate mass fraction along vertical lines at x/D=0.5 (red line), 0.8 (blue line) and 1.0 (green line) for ϕ=6.2, respectively. Initial degree of supersaturation at stagnation point downstream of the nozzle exit is S_{0b}=0.8. As seen from this figure, condensate mass fraction expands over the radial direction and the maximum values of condensate mass fraction become large with an increase of distance from nozzle exit.

Figure 7 shows time-averaged distributions of displacement thickness on flat plate for ϕ=6.2(Case 3 and Case 4). Initial degrees of supersaturation at stagnation point downstream of the nozzle exit is S_{0b}=0 (red line) and S_{0b}=0.8 (blue line). As seen from this figure, in the case of case 4 (moist air), displacement thickness on the flat plate is large in comparison with case 3(dry air). This is considered to be due to the increase of dynamic viscosity (decrease of Reynolds number) by non-equilibrium condensation.

5. Conclusions

A numerical study has been made to investigate the effect of non-equilibrium condensation occurred in the share layer on characteristics of an impinging supersonic jet. The results obtained are summarized as follows :

(1) Simulated results were good agreement with experimental results.
(2) In the case of dry air discharged to atmosphere with moisture, non-equilibrium condensation occurred in the shear layer of supersonic jet.
(3) Non-equilibrium condensation in shear layer decreased the static pressure on flat plate.
(4) Non-equilibrium condensation in shear layer increased the displacement thickness on flat plate.

References

[1] Lamont P.J., Hunt B.L. The Impinging of Underexpanded Axisymmetric Jets on Perpendicular and Inclined Flat Plates. Journal of Fluid Mechanics. 1980;100(Part 3):471-511.
[2] Kalghatgi G.T., Hunt B.L. The Occurrence of Stagnation Bubbles in Supersonic Jet Impingement Flows. Aeronautical Quarterly. 1976;27:169-185.
[3] Masuda W., Moriyama E. Aerodynamic Characteristics of Underexpanded Coaxial Impinging Jets. JSME International Journal. Series B. 1994;37(4):769-775.
[4] Wegener, P.P., Mack L.M. Condensation in Supersonic Hypersonic Wind Tunnels. Adv. in Appl. Mech. 1958;5.
[5] Matsuo K, Kawagoe S. Sonoda K. et al. Studies of Condensation Shock Waves (Part 1, Mechanism of Their Formulation). Bulletin of JSME. 1985;28:2577-2582.
[6] Sakakibara Y., Iwamoto Y. Numerical Study of Oscillation Mechanism in Underexpanded Jet Impinging on Plate. Journal of Fluid Engineering. 1998;120:477-481.
[7] Bird R.B, Stewart W.E, Lightfoot E.N. Transport Phenomena. Wiley. New York;1960
[8] Hirschfelder J.O, Curtiss C.F, Bird R.B. Molecular Theory of Gases and Liquids. Wiley. New York;1954.
[9] Wilcox D.C. Formulation of the *k*-ω Turbulence Model Revisited. AIAA Journal;2008:46(11):2823-2838.
[10] Yee, H.C. A Class of High-resolution explicit and implicit shock capturing methods. NASA-TM-89464.
[11] Strang G., 1976. Linear Algebra and Its Applications, Massachusetts Institute of Technology.

Available online at www.sciencedirect.com

SciVerse ScienceDirect

Procedia Engineering 00 (2012) 000–000

Procedia Engineering

www.elsevier.com/locate/procedia

5th BSME International Conference on Thermal Engineering

Effect of local occurrence of non-equilibrium condensation on transonic flow field

Shigeru Matsuo[a]*, A. B. M. Toufique Hasan[b], Junji Nagao[c], Tokitada Hashimoto[a], Toshiaki Setoguchi[d], Heuy Dong Kim[e]

[a]*Department of Advanced Technology Fusion, Saga University, 1 Honjo-machi, Saga 840-8502, Japan*
[b]*Department of Mechanical Engineering, Bangladesh University of Engineering & Technology, Dhaka 1000, Bangladesh*
[c]*Graduate School of Science & Engineering, Saga University, 1 Honjo-machi, Saga-shi, Saga 840-8502, Japan*
[d]*Institute of Ocean Energy, Saga University, 1 Honjo-machi, Saga-shi, Saga 840-8502, Japan*
[e]*School of Mechanical Engineering, Andong National University, 388 Song Cheon Dong, Andong 760-749, Korea n*

Abstract

The transonic flow over an airfoil is characterized by a shock wave standing on the suction surface. When non-equilibrium condensation occurs in a supersonic flow field, the flow is affected by latent heat released by it. According to previous works, it was found that the occurrence of non-equilibrium condensation just before the shock wave led to reduction of shock strength. In these studies, non-equilibrium condensation occurs across the passage of the nozzle and it causes the total pressure loss in the flow field. However, local occurrence of non-equilibrium condensation in the flow field may change the characteristics of total pressure loss compared with that by non-equilibrium condensation across the passage of the nozzle and there are few for researches of locally occurred non-equilibrium condensation in a transonic flow field. The purpose of this study is to clarify the effect of local occurrence of non-equilibrium condensation on transonic flow field with a circular bump. As a result, shock strength and total pressure loss decrease with a decrease of generation region of condensate droplets.

Keywords: Compressible flow, Shock wave, Control, Transonic Flow, Non-equilibrium Condensation, Simulation

Nomenclature

C_p	specific heat at constant pressure (J/kg·K)
E, F	numerical flux
g	condensate mass fraction
H	source term of turbulence
*H**	height of nozzle throat
I	nucleation rate ($1/(m^3K)$)
k	specific turbulence kinetic energy
L	distance from throat (m)
M	Mach number
p	static pressure (Pa)
Q	source term of condensation

* Corresponding author. Tel.: +81-952-28-8606; fax: +81-952-28-8687.
E-mail address: matsuo@me.saga-u.ac.jp

R, S	Source term of vicosity
R	radius of wall curvature (m)
S	initial degree of supersaturation
U	conservation mass term
x, y	Cartesian coordinate
Greek symbols	
β	integrated total pressure loss
δ^*	displacement thickness (m)
ϕ	shock strength
μ	molecular viscosity (Pa·s)
ρ	density (kg/m^3)
τ	shear stress (Pa)
ω	specific dissipation rate
Subscripts	
0	stagnation point
0t	stagnation point at tank
1	vapor
2	dry air
t	turbulence

1. Introduction

The characteristics of transonic flow over an airfoil are determined by a shock wave standing on the suction surface. In this case, the shock wave/boundary layer interaction becomes complex because an adverse pressure gradient is imposed by the shock wave on the boundary layer. Several types of passive control techniques have been applied to shock wave/boundary layer interaction in the transonic flow. For instance, Bahi et al., 1983 and Raghunathan, 1988 described that a porous wall and cavity system, when it was applied at the foot of the shock wave, were known to be effective in alleviating undesirable adverse pressure gradient of the shock wave/boundary layer interaction. However, this control method essentially leads to large viscous losses caused by the porous walls, which can overcompensate the control benefit of the shock wave. Thus, the method can not be generalized as an effective method.

In order to overcome the demerits above several techniques were proposed. Firstly, the passive control using the porous wall with a cavity and vortex generator was applied to the shock wave/boundary layer interaction. It was shown by Saida et al., 2002 that this method was effective to the reduction of the wave drag and suppression of the boundary layer growth. Second, Raghunathan et al., 1999, O'Rourke et al., 2001 reported that the passive control using the porous wall with a cavity and vortex control jets upstream of porous wall might be effective to control of the shock position and pressure gradient. Ogawa et al., 2006 described that there are the optimum flow deflection for maximum reduction of total pressure losses in the flow with shock wave theoretically when the flow direction are changed by control device. Furthermore, possibilities for the control of flow fields due to non-equilibrium condensation have been shown so far (Wegener et al., 1958, Matsuo et al., 1985, Schnerr, 1986, Setoguchi et al., 1997, Matsuo et al., 1997). Furthermore, the development of boundary layer was reduced behind the shock wave. In these flow fields, non-equilibrium condensation occurs across the passage of the nozzle and it causes the total pressure loss in the flow field.

However, local occurrence of non-equilibrium condensation in the flow field may change the characteristics of total pressure loss compared with that by non-equilibrium condensation across the passage of flow field. Nagao, et al., 2012 described that locally occurred non-equilibrium condensation in supersonic nozzle reduces the total pressure loss in comparison with that occurred across the passage of the nozzle. However, there are few for researches of locally occurred non-equilibrium condensation in a transonic flow field.

The purpose of this study is to clarify the effect of locally occurred non-equilibrium condensation on the shock strength and total pressure loss on a transonic internal flow field with a circular bump.

2. Experimental Setup and Procedure

To validate simulated results, static pressures on the wall were measured and the flow was visualized by schlieren optical method. Figure 1(a) shows the experimental apparatus. The apparatus is consisted of reservoir tank, air drier, test section,

valves and vacuum tank. Figure 1(b) shows the details of test section. Height of the nozzle is 60 mm. A radius of circular arc is 100 mm. The height of throat is 56 mm. Dry air (S_0=0.18) is used as a working gas. Total pressure and temperature of reservoir tank are 102 kPa and 296 K, respectively.

3. Computational Conditions

Figure 2 shows a computational domain of the transonic flow field and boundary condition. The nozzle has a height of H=60 mm at the inlet and exit, and a radius of circular arc is R =100 mm. The height of nozzle throat H* is 56 mm. The region upstream of the nozzle was separated into dry air and moist air regions by a plate. Thickness of the plate is 0 mm.

Table 1 shows initial conditions used in the present calculation. Total pressure p_0 and temperature T_0 at stagnation point are 102 kPa and 298 K, respectively. The working gases of upper and lower sides of the plate are dry and moist airs, respectively. The plate position h/H is 0 (Case 1), 1.0 (Case 2), 0.125 (Case 3). The initial degree of supersaturation S_0 of moist air is 0.8. The number of grids is 450×119.

The adiabatic no-slip wall was used as boundary condition. The boundary condition of inlet and exit were fixed at initial condition and out flow condition, respectively. Condensate mass fraction g was set at g=0 on the wall.

4. CFD Analysis

The governing equations, i.e., the unsteady 2D compressible Navier-Stokes equations that were combined with continuity, energy, nucleation rate, a droplet growth and diffusion equations (Bird et al., 1983, Hirschfelder, 1954) were written in

$$\frac{\partial \boldsymbol{U}}{\partial t}+\frac{\partial \boldsymbol{E}}{\partial \xi}+\frac{\partial \boldsymbol{F}}{\partial \eta}=\frac{1}{Re}\left(\frac{\partial \boldsymbol{R}}{\partial \xi}+\frac{\partial \boldsymbol{S}}{\partial \eta}\right)+\boldsymbol{H}+\boldsymbol{Q} \tag{1}$$

where

$$\boldsymbol{U}=\frac{1}{J}\begin{bmatrix}\rho\\ \rho u\\ \rho v\\ E_t\\ \rho k\\ \rho\omega\\ \rho g\\ \rho D_1\\ \rho D_2\\ \rho D_3\\ \rho_1\end{bmatrix},\ \boldsymbol{E}=\frac{1}{J}\begin{bmatrix}\rho U\\ \rho uU+\xi_x p\\ \rho vU+\xi_y p\\ (E+p)U\\ \rho kU\\ \rho\omega U\\ \rho gU\\ \rho D_1U\\ \rho D_2U\\ \rho D_3U\\ \rho_1U\end{bmatrix},\ \boldsymbol{F}=\frac{1}{J}\begin{bmatrix}\rho V\\ \rho uV+\eta_x p\\ \rho vV+\eta_y p\\ (E+p)V\\ \rho kV\\ \rho\omega V\\ \rho gV\\ \rho D_1V\\ \rho D_2V\\ \rho D_3V\\ \rho_1V\end{bmatrix}$$

$$\boldsymbol{R}=\frac{1}{J}\begin{bmatrix}0\\ \xi_x\tau_{xx}+\xi_y\tau_{xy}\\ \xi_x\tau_{xy}+\xi_y\tau_{yy}\\ \tau_{E,\xi}\\ f_k\left(\xi_x\frac{\partial k}{\partial x}+\xi_y\frac{\partial k}{\partial y}\right)\\ f_\omega\left(\xi_x\frac{\partial \omega}{\partial x}+\xi_y\frac{\partial \omega}{\partial y}\right)\\ 0\\ 0\\ 0\\ 0\\ \tau_{c1,\xi}\end{bmatrix},\ \boldsymbol{S}=\frac{1}{J}\begin{bmatrix}0\\ \eta_x\tau_{xx}+\eta_y\tau_{xy}\\ \eta_x\tau_{yx}+\eta_y\tau_{yy}\\ \tau_{E,\eta}\\ f_k\left(\eta_x\frac{\partial k}{\partial y}+\eta_y\frac{\partial k}{\partial y}\right)\\ f_\omega\left(\eta_x\frac{\partial \omega}{\partial y}+\eta_y\frac{\partial \omega}{\partial y}\right)\\ 0\\ 0\\ 0\\ 0\\ \tau_{c1,\eta}\end{bmatrix},\ \boldsymbol{H}=\frac{1}{J}\begin{bmatrix}0\\ 0\\ 0\\ 0\\ P_k-\beta^*\rho\omega k\\ f_{\mathrm{H}}\\ 0\\ 0\\ 0\\ 0\\ 0\end{bmatrix},\ \boldsymbol{Q}=\frac{1}{J}\begin{bmatrix}0\\ 0\\ 0\\ 0\\ 0\\ 0\\ \rho\dot{g}\\ \rho D_1\\ \rho D_2\\ \rho D_3\\ 0\end{bmatrix} \tag{2}$$

In Eq.(1), ***U*** is conservative vector, ***E*** and ***F*** are inviscid flux vector and ***R*** and ***S*** are viscous flux vectors. *H* and ***Q*** are the source terms corresponding to turbulence and condensation, respectively. τ_{xx}, τ_{xy}, τ_{yx} and τ_{yy} are components of viscous shear stress.

In Eq.(2),

$$\tau_{E,\xi} = \xi_x\left(q_x + u\tau_{xx} + v\tau_{xy}\right) + \xi_y\left(q_y + u\tau_{yx} + v\tau_{yy}\right),\ \tau_{E,\eta} = \eta_x\left(q_x + u\tau_{xx} + v\tau_{xy}\right) + \eta_y\left(q_y + u\tau_{yx} + v\tau_{yy}\right) \tag{3}$$

$$\tau_{c1,\xi} = \xi_x\left(\rho_1\Delta_1\frac{\partial c_1}{\partial x}\right) + \xi_y\left(\rho\Delta_1\frac{\partial c_1}{\partial y}\right),\ \tau_{c1,\eta} = \eta_x\left(\rho_1\Delta_1\frac{\partial c_1}{\partial x}\right) + \eta_y\left(\rho\Delta_1\frac{\partial c_1}{\partial y}\right) \tag{4}$$

$$q_{x_j} = \frac{1}{\gamma - 1}\left(\frac{\mu}{Pr} + \frac{\mu_t}{Pr_{\mathrm{t}}}\right)\frac{\partial T}{\partial x_{\mathrm{j}}} + \rho\left(h_1\Delta_1\frac{\partial c_1}{\partial x_{\mathrm{j}}} + h_2\Delta_2\frac{\partial c_2}{\partial x_{\mathrm{j}}}\right) \tag{5}$$

$$f_k = \mu + \sigma^*\frac{\rho k}{\omega},\ f_\omega = \mu + \sigma\frac{\rho k}{\omega},\ f_{\mathrm{H}} = \alpha\frac{\omega}{k}P_{\mathrm{k}} - \beta\rho\omega^2 + \sigma_{\mathrm{d}}\frac{\rho}{\omega}\left(\frac{\partial k}{\partial x}\frac{\partial \omega}{\partial x} + \frac{\partial k}{\partial y}\frac{\partial \omega}{\partial y}\right) \tag{6}$$

$$P_{\mathrm{k}} = 2\mu_{\mathrm{t}}\left[\left(\frac{\partial u}{\partial x}\right)^2 + \frac{1}{2}\left(\frac{\partial v}{\partial x} + \frac{\partial u}{\partial y}\right) + \left(\frac{\partial v}{\partial y}\right)^2\right],\ \mu_{\mathrm{t}} = \frac{\rho k}{\tilde{\omega}},\ \tilde{\omega} = \max\left\{\sqrt{\frac{2\bar{S}_{\mathrm{i,j}}\bar{S}_{\mathrm{i,j}}}{\beta^*}}\right\} \tag{7}$$

$$\bar{S}_{\mathrm{i,j}} = S_{\mathrm{i,j}} - \frac{1}{3}\frac{\partial u_{\mathrm{k}}}{\partial x_{\mathrm{k}}},\ S_{\mathrm{i,j}} = \frac{1}{2}\left(\frac{\partial u_{\mathrm{i}}}{\partial x_{\mathrm{j}}} + \frac{\partial u_{\mathrm{j}}}{\partial x_{\mathrm{i}}}\right) \tag{8}$$

The density of gas mixture is calculated by the sum of density of vapor (ρ_1) and dry air (ρ_2) ；

$$\rho = \rho_1 + \rho_2 \tag{9}$$

The mass fraction can be given as

$$c_{\mathrm{i}} = \frac{\rho_{\mathrm{i}}}{\rho} \tag{10}$$

In equations (4) and (5) Δ_1 and Δ_2 are effective diffusivities. The closure coefficients are,

$$\beta = 0.0708,\ \alpha = \frac{13}{25},\ \beta^* = \frac{9}{100},\ \sigma = \frac{1}{2},\ \sigma^* = \frac{3}{5},\ Pr_{\mathrm{t}} = \frac{7}{8} \tag{11}$$

$$\sigma_{\mathrm{d}} = \begin{cases} 0, & \dfrac{\partial k}{\partial x_{\mathrm{j}}}\dfrac{\partial \omega}{\partial x_{\mathrm{j}}} \le 0 \\ \sigma_{\mathrm{d0}}, & \dfrac{\partial k}{\partial x_{\mathrm{j}}}\dfrac{\partial \omega}{\partial x_{\mathrm{j}}} \ge 0 \quad \left(\sigma_{\mathrm{d0}} = \dfrac{1}{8}\right) \end{cases} \tag{12}$$

The governing equation systems that are non-dimensionalized with reference values at the reservoir condition were mapped from the physical plane into a computational plane of general transform. To close the governing equations, *k*-ω model (Wilcox, 2008) was employed in computations. A third-order TVD finite difference scheme with MUSCL (Yee, 1989) was used to discretize the spatial derivatives, and second-order central difference scheme for the viscous term, and a second-order fractional step method (Strang, 1976) was employed for time integration.

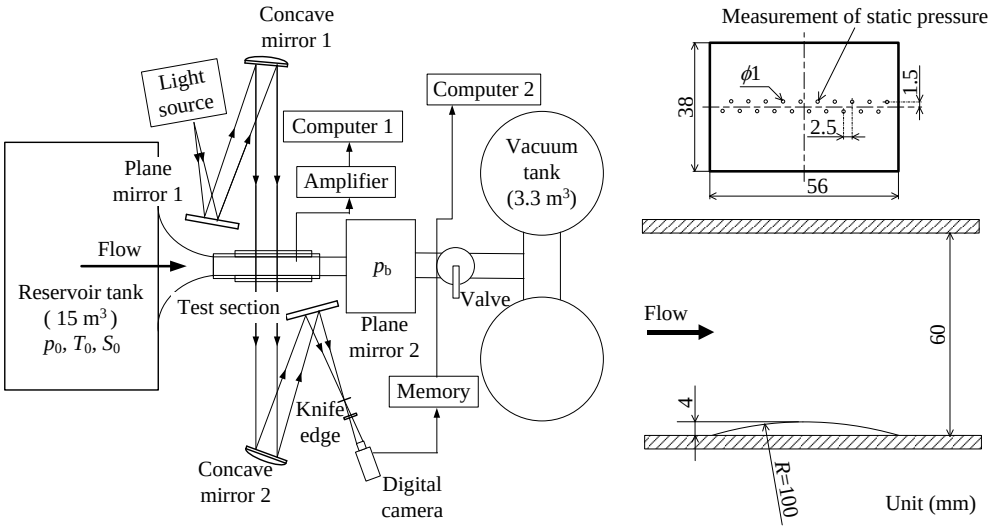

(a) Experimental apparatus (b) Details of test section

Fig. 1. Experimental apparatus and details of test section

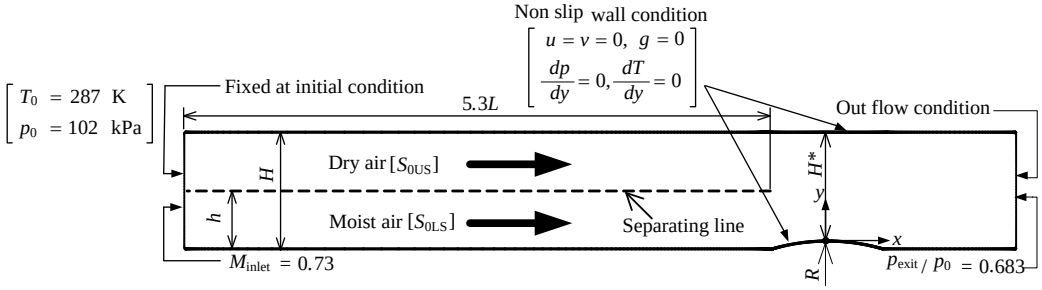

Fig. 2. Computational domain and boundary conditions

Table 1. Computational conditions

	h/H	Initial degree of supersaturation S_{0US}	S_{0LS}	p_0 [kPa]	T_0 [K]
Case 1	0				
Case 2	1.0	0	0.8	102	298
Case 3	0.125				

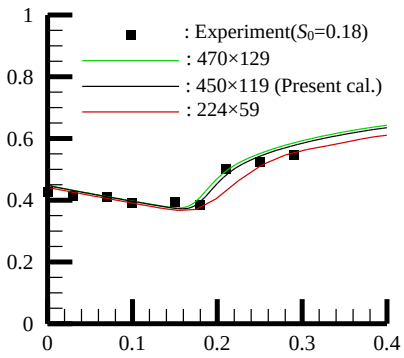

Fig. 3. Comparison of static pressures distributions between the experimental and simulated flow fields ($S_0 = 0$)

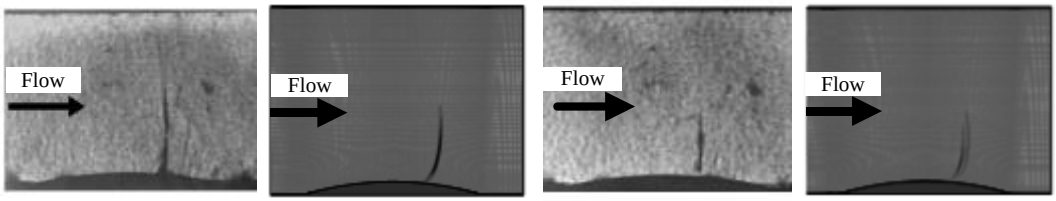

(a) Experiment (S_0=0.18) (b) Simulation (S_0=0.0) (c) Experiment (S_0=0.5) (d) Simulation (S_0=0.5)

Fig. 4. Comparison of schlieren photographs between the experimental and simulated flow fields

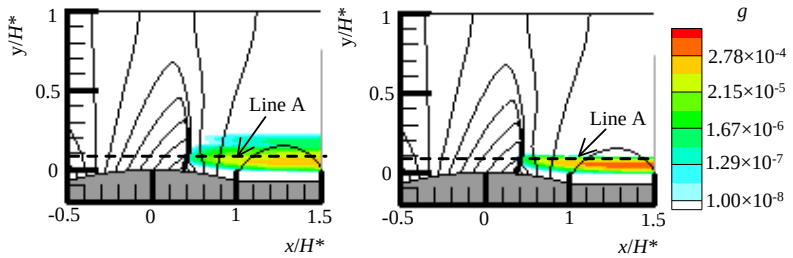

(a) Case 2 (h/H=1) (b) Case 3 (h/H=0.125)

Fig. 5. Time-averaged contour maps of static pressure p/p_0 (solid line) and condensate mass fraction g (color)

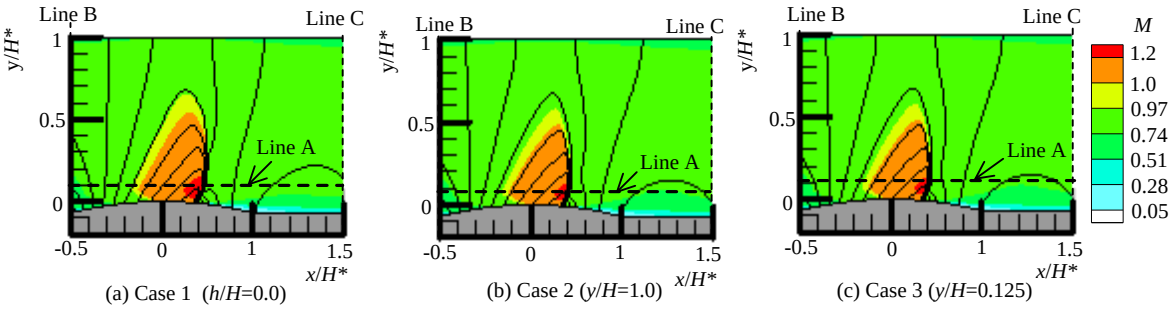

(a) Case 1 (h/H=0.0) (b) Case 2 (y/H=1.0) (c) Case 3 (y/H=0.125)

Fig. 6. Time-averaged contour maps of static pressure p/p_0 (solid line) and Mach number M (color)

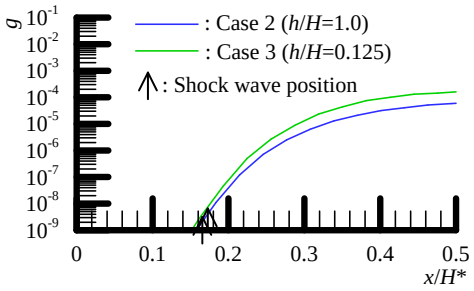

Fig. 7. Time-averaged distributions of condensate mass fraction g on line A

5. Result and discussions

Figure 3 shows comparison of static pressure distributions on lower wall obtained by experiment and simulation in case of dry air. Values of initial degree of supersaturation for experiment and simulation are S_0=0 and 0.18, respectively. As is evident from this figure, results of the number of grids of 450×119 and 470×129 are good agreement well with experimental result. Therefore, the number of grids of 450×119 was adopted in order to prevent the consumption of computation time in the present study.

Figure 4 shows comparison between experimental and simulated results in cases of dry air (Experiment : S_0=0.18 (Fig.4(a)), Simulation : S_0=0 (Fig.4(b))) and moist air (S_0=0.5 (Experiment : Fig.4(c), Simulation : 4(d)), respectively. Flow direction is left to right. As seen from these figures, shock wave is observed on the circular arc bump. In the case of dry air (Figures 3(a)

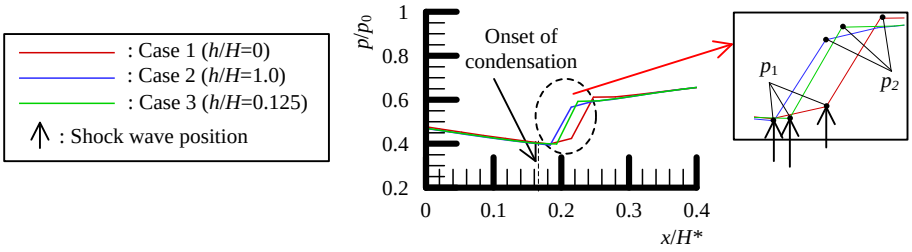

Fig. 7. Time-averaged distributions of static pressure p/p_0 on line A

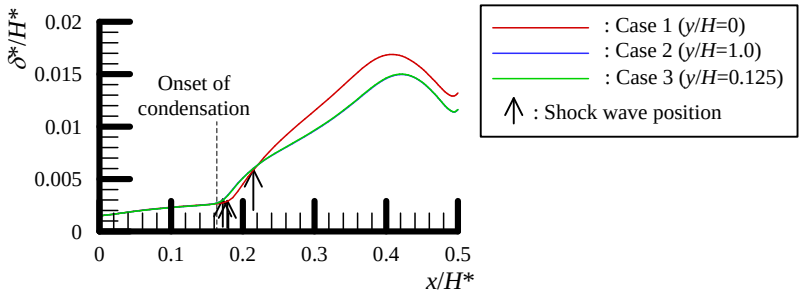

Fig. 8. Time-averaged distributions of displacement thickness δ^*/H^*

Table 2. Shock strength ϕ

	Shock strength ϕ	$(\phi-\phi_{Case1})/\phi_{Case1}\times100$ %
Case 1	1.48	0
Case 2	1.43	-3.5
Case 3	1.44	-2.7

Table 3. Integrated total pressure loss β

	Integrated total pressure loss $\beta\times10^{-2}$	$(\beta-\beta_{dd})/\beta_{dd}\times100$ %
Case 1	9.60	0
Case 2	4.50	-53.1
Case 3	4.04	-57.9

and (b)), shock wave is clearly visible compared with that of moist air (Figures 3(c) and (d)). Further, simulated results agree well with experimental results.

Figures 5(a) and (b) show time-averaged contour maps of static pressure p/p_0 (solid line) and condensate mass fraction g for Cases 2 and 3, respectively. Initial degree of supersaturation of moist air is S_0=0.8. Regions of moist air for Cases 2(Fig. 5(a)) and 3(Fig. 5(b)) are h/H=1.0 and 0.125, respectively. As seen from these figures, condensate droplets are observed and condensate mass fraction begins to increase along the bump wall side upstream of the shock wave and distributes over downstream region. For Case 3 (Fig. 5(b)), condensate droplets expand in a narrow region compared with that of Case 2 (Fig. 5(a)).

Figures 6(a), (b) and (c) show the time-averaged contour maps of static pressure p/p_0 (solid line) and Mach number M for Cases 1, 2 and 3, respectively. As seen from these figures, a shock wave is shown in the flow field. For Cases 2 (Fig. 6(b)) and 3(Fig. 6(c)), the height of adiabatic shock wave seems to be small compared with that for Case 1 (Fig. 6(a)). It is considered for the reason that Mach number just before shock wave reduces due to the condensation.

Figure 7 shows time-averaged distributions of condensate mass fraction g on line A for Cases 2 and 3, respectively. The abscissa is the distance x/H^* from throat, and the ordinate is condensate mass fraction g. As seen from this figure,

condensate mass fraction begins to increase before the shock wave (x/H^*=0.16). In the case of Case 3, condensate mass fraction increases rapidly and maximum value is large in comparison with that for Case 2.

Figure 8 shows time-averaged distributions of static pressure p/p_0 on line A for all cases. The abscissa is the distance x/H^* from throat, and the ordinate is static pressure p/p_0. As seen from this figure, static pressure begins to increase after the onset of condensation. In cases of Cases 2 and 3, the position of shock wave is located upstream compared with that of Case 4. This is due to reduction of Mach number before the shock wave by non- equilibrium condensation. Further, the position of shock wave for Case 2 is located upstream compared with that for Case 3.

Figure 9 shows time-averaged distributions of displacement thickness δ^*/H^* for all cases. The abscissa is the distance x/H^* from throat, and the ordinate is displacement thickness δ^*/H^*. As is evident from this figure, displacement thickness behind the shock wave for Cases 2 and 3 are small compared with that for Case 1 (no condensation).

Table 2 shows ratio of p_2 to p_1 as indicated in Fig. 6 (shock strength $\phi = p_2/p_1$) and change in ϕ based on shock strength ϕ_{Case1} in case without condensation (Case 1) for all cases. As seen from this table, shock strengths for Cases 2 and 3 are small in comparison with that for Case 1. The strengths for Cases 2 and 3 are reduced by 3.5 % and 2.7 %, respectively.

Table 3 shows integrated total pressure loss β from Line B to Line C as shown in Figs. 3 and 4 and change in β based on integrated total pressure loss β_{dd} in case without condensation (Case 1). Integrated total pressure loss is calculated from following equation.

$$\beta = \int_{\text{Lower wall}}^{\text{Upper wall}} \left(1 - \frac{p_{01}}{p_0} \right) dy \tag{13}$$

In Eq. (15), p_{01} and p_0 are local and stagnation total pressure, respectively. As is evident from this table, integrated total pressure losses for Cases 2 and 3 are small compared with that for Case 1 and integrated total pressure loss for Case 3 is the smallest. This reason is considered that the region of non-equilibrium condensation for Case 3 is small compared with that for Case 2.

6. Conclusions

A numerical study has been made to investigate the effect of locally occurred non-equilibrium condensation on a transonic flow field with circular arc bump. The results obtained are summarized as follow :

(1) Adiabatic shock wave moved upstream by locally occurred non-equilibrium condensation.
(2) Displacement of adiabatic shock wave position decreased with a decrease of occurrence region of condensate droplets.
(3) Displacement thickness with local occurrence of non-equilibrium condensation became thin downstream compared with that of no condensation.
(4) Shock strength in case with local occurrence of non-equilibrium condensation was small compared with that of no condensation.
(5) Total pressure loss of the flow field decreased with a decrease of occurrence region of condensate droplets.

References

[1] Bahi L, Ross J M, Nagamatsu T., 1983. Passive shock wave/boundary layer control for transonic supercritical aerofoil drag reduction., AIAA-83-0137.
[2] Raghunathan S., 1988. Passive control of shock-boundary layer interaction., Prog. Aerospace Sci., Vol.25 , pp.271-296.
[3] Saida N, Tomizuka Y., 2002. Passive Control of Oblique Shock/Boundary Layer Interaction, Proc. of Symposium on Shock Waves Japan 2002., Tokyo(Japan),.
[4] Raghunathan S R, O'Rourke M, Watterson J K, et al.., 1999. Passive Vortex Control Jets for Shock Boundary Layer Interactions, AIAA-99-3196.
[5] O'Rourke M J, Healy M, Raghunathan, S R., 2001. Computational Experiment Investigating Passive Vortex Control Jets for Shock Boundary Layer Interactions, AIAA-2001-3028.
[6] Ogawa H. and Babinsky H., 2006, Evaluation of wave drag reduction by flow control, Aerospace Science and Technology, Vol. 10, No. 1, pp.1-8.
[7] Wegener P P, Mach L M., 1958. Condensation in Supersonic Hypersonic Wind Tunnels., Advances in Appl. Mech., Vol.5, pp.307-447.
[8] Matsuo K, Kawagoe S, Sonoda K, et al., 1985. Studies of Condensation Shock Waves (Part 1), Mechanism of their Formulation). Bulletin of JSME, Vol.28, No.241, pp.1416-1422.
[9] Schnerr G H., 1986. Homogene Kondensation in Stationären Transsonischen Strömungen Durch Lavaldüsen und um Profile, Habilitationsschrift. Universität Karlsruhe (TH), Germany.
[10] Setoguchi T, Matsuo S, Yu S., 1997. Effect of Homogeneous Condensation on Flow Fields in a Supersonic Nozzle., J. of Thermal Science., Vol.6, No.4, Vol.6, No.2, pp.90-96.
[11] Matsuo S, Setoguchi T, Yu S, et al., 1997. Effect of Nonequilibrium Condensation of Moist Air on the Boundary Layer in a Supersonic Nozzle., J. of Thermal Science., Vol.6, No.4, pp.260-272.

[12] Nagao J., Matsuo, S., Setoguchi, Kim H.D., 2012. Effect of Local Occurrence of Non-Equilibrium Condensation on Flow Fields in a Supersonic Nozzle, Thermal and Fluids Engineering Conference (TFEC8 2012), 18-21 March, GSF23-001, Incheon (Korea).
[13] Bird R.B, Stewart W.E, Lightfoot E.N., 1960. Transport Phenomena, Wiley., New York.
[14] Hirschfelder J.O, Curtiss C.F, Bird R.B., 1954, Molecular Theory of Gases and Liquids, Wiley., New York.
[15] Wilcox D.C., 2008. Formulation of the *k*-ω Turbulence Model Revisited., AIAA Journal., Vol.46, No.11, pp.2823-2838.
[16] Yee, H.C., A Class of High-resolution explicit and implicit shock capturing methods., NASA-TM-89464.
[17] Strang G., 1976. Linear Algebra and Its Applications, Massachusetts Institute of Technology.

Available online at www.sciencedirect.com

SciVerse ScienceDirect

Procedia Engineering 00 (2012) 000–000

Procedia Engineering

www.elsevier.com/locate/procedia

5th BSME International Conference on Thermal Engineering

Flashing flow of subcooled liquid through small cracks

S.T.Revankar[a,b,*], B. Wolf[a], J. R. Riznic[c]

[a]*School of Nuclear Engineering, Purdue University, West Lafayette, IN, USA*
[b]*Division of Advanced Nuclear Engineering, POSTECH, Pohang, Gyungbuk, Republic of Korea*
[c]*Canadian Nuclear Safety Commission, 280 Slater, P.O.B. 1046, Station B Ottawa, Ontario K1P5S9 Canada*

Abstract

In Pressurized Water Reactors and in CANDU reactors steam generator (SG) tubes represent a major fraction of the reactor primary coolant pressure boundary. The ability to estimate the leak rates from the through wall cracks in the steam generator tube is important in terms of radiological source terms and overall operational management of steam generators as well as demonstration of the leak-before-break condition. In this study an experimental program and analysis methods were developed to measure and assess the choking flow rate of subcooled water through simulated steam generator tube crack geometries. Experiments were conducted on choking flow for various simulated crack geometries for vessel pressures up to 7 MPa with various subcoolings. Measurements were done on subcooled flashing flow rate through well defined simulated crack geometries with L/D<5.5. Both homogeneous equilibrium and non-equilibrium mechanistic models were developed to model two-phase choking flow through slits. A comparison of the model results with experimental data shows that the HE based models grossly under predict choking flow rates in such geometries, while homogeneous non-equilibrium models greatly increase the accuracy of the predictions.

Keywords: flashing flow; choking flow; steam genertor tube; cracks,; experiments; Burnel model.

1. Introduction

In Pressurized Water Reactors and in CANDU reactors steam generator (SG) tubes represent a major fraction of the reactor primary coolant pressure boundary. The ability to estimate the leak rates from the through wall cracks in the steam generator tube is important in terms of radiological source terms and overall operational management of steam generators as well as demonstration of the leak-before-break condition. In this study an experimental program and analysis methods were developed to measure and assess the choking flow rate of subcooled water through simulated steam generator tube crack geometries. Experiments were conducted on choking flow for various simulated crack geometries for vessel pressures up to 7 MPa with various subcoolings. Measurements were done on subcooled flashing flow rate through well defined simulated crack geometries with L/D<5.5. Both homogeneous equilibrium and non-equilibrium mechanistic models were developed to model two-phase choking flow through slits. A comparison of the model results with experimental data shows that the HE based models grossly under predict choking flow rates in such geometries, while homogeneous non-equilibrium models greatly increase the accuracy of the predictions

The steam generator (SG) tubes represent a major fraction of the reactor primary coolant pressure boundary surface area in both CANDU reactors and Pressurized Water Reactors (PWR). These tubes have an important safety role because

* Corresponding author. Tel.: +82-54-279-9560; fax: +82-54-279-9559.
E-mail address: shripad@postech.ac.kr

they constitute one of the primary barriers between the radioactive and non-radioactive sides of the plant. The integrity of SG tubes is a safety-related issue, since the tubes are susceptible to corrosion and damage. The ability to estimate the leak rates from the through wall cracks in the steam generator tube is important in terms of radiological source terms and overall operational management of steam generators as well as demonstration of the leak-before-break condition. There are many identified degradation mechanisms related to SG tubes which include; intergranular attack and outside diameter stress corrosion cracking (SCC), primary water stress corrosion cracking, tube fretting and wear, foreign material wear, pitting, high cycle fatigue, and wastage or thinning. Of these, environmentally induced degradation through intergranular SCC and intergranular attack is the most serious degradation process at present. This degradation commonly occurs in crevice regions at tube support plates and tube sheet locations or under sludge piles, although intergranular SCC has also been observed in the free span of the tubes.

Damage to a steam generator tube impairs its ability to perform its required safety function in terms of both structural integrity and leakage integrity. They must maintain more than 6.9 MPa pressure differential between the inside and outside tube wall during normal operation. In the event of a main steam line break (MSLB) where the secondary side drops to atmospheric pressure, the tube wall differential pressure can be more than double that of normal operation. Traditionally, steam generators and steam generator tubes were designed with a sufficient safety margin against rupture. The design requirements of ASME code and the Nuclear Regulatory Commission (NRC) for steam generator tubes is $1.4\Delta P_{MSLR} > 25$ MPa [1]. These safety margins are based on the rupture or burst pressure of an unflawed tube. A typical unflawed Alloy 600 tube has an industry expected burst pressure of ~86 MPa [2].

A sufficient safety margin in design against tube rupture was originally the basis to maintaining a suitable level of plant safety and reliability. Steam generator operability requires the completion of steam generator tube inspections using non-destructive techniques, usually eddy current examination, in intervals ranging from 12 to 40 months. There are also further steam generator tube integrity assessment guidelines which provide assessment procedures and criteria for assessing tube integrity for burst/collapse and through wall leakage, loading definitions, and design margins [3]. The final result is that steam generators operate under the leak-before-break concept, which demonstrates that a crack can grow through-wall, resulting in a leak, and that this through-wall flaw will be detected by leakage monitoring systems well before the flaw becomes unstable and the tube ruptures. Much research in the area of steam generator tube integrity is therefore related to the burst characterization of tubes with flaws [4]. Literature survey shows that most of the data on simulated steam generator cracks is carried out with the tube ultimately leading to burst [5]. The break geometry characterization is not properly carried out to associate the discharge data with a well characterized break. Thus prediction and benchmarking the predictions of leak rates through SG cracks with data is challenging.

There is very limited data on the steam generator tube leak rate measurement. Most studies of subcooled choking flow are related to long tubes with large L/D and nozzles [6-8]. The survey shows that this geometry has been studied over a large range of pressures and liquid subcoolings however, as can be seen, these data focus on L/D geometries greater than 15. Also, all of those data have a channel length greater than 10 mm, which is not indicative of steam generator tubing. Steam generator tubes have a wall thickness typically less than 3 mm. In view of this an experimental program was carried out where the simulated steam generator tube crack geometry were well characterized and choking flow of subcooled water tests were performed.

2. Experimental Facility

Design of a test facility to measure leak rates of through-wall cracks was based on the following goals. (1) The test facility should be modular so that various crack geometries can be studied. (2) The pressure differential across the break should be similar to the prototype about 6.8 MPa (1000 psi). (3) Facility should be such that tests can be easily repeated. Based on these goals a test facility is designed. A schematic of the test facility can be seen in Figure 1.

2.1. Pressure Vessel

The pressure vessel was constructed from a single 3.5 inch diameter schedule 160 316SS seamless pipe. It is 3.05 m in length and has numerous inlet and outlet ports including a 1 inch NPT port for connection to the test section specimens and ¼ inch ports for pressure measurement and thermocouples. .

The vessel is equipped with one pressure relief valve with manufacturer preset of 8.3 MPa. The pressure vessel is pressurized using compressed nitrogen bottles connected via 3/8 inch SS tubing. A single stage regulator with downstream pressure gauge range of 0-13.8 MPa is used to keep a constant regulated pressure during a given experimental run.

2.2. Pressure Measurement

One differential pressure transducer and one gauge pressure transmitter are used for pressure data acquisition. The differential pressure transducer is a Honeywell ST3000® smart transducer used to measure the water level in the pressure vessel. A gauge pressure transmitter, located at P2 in Fig. 1 is used to measure the pressure just before the choking plane. The transmitter was manufactured and calibrated by Ashcroft®, with a range of 0-13.8 MPa with accuracy of 1.0%. Other pressure measurements are also available through needle gauges. As stated above, there is a pressure gauge on the nitrogen regulator. Also, a WIKA® brand needle gauge with a range of 0-6.9 MPa is located at P1. This allows for redundant monitoring of the vessel pressure.

2.3. Vessel Heating

Due to the high pressure and temperature at the extreme end of the range of experiments performed, submersible type heaters were not able to be used. The vessel water was heated from outside the pressure vessel using three band heaters 3 inches wide with and I.D. of 4.5 inches. The band heaters are Watlow® brand thin band ceramic insulated heaters. Each heater is capable of producing 1200 Watts and run in parallel off a 240 volt power supply. The entire pressure vessel and piping to the test section are insulated with 2 inches of mineral wool variety insulation.

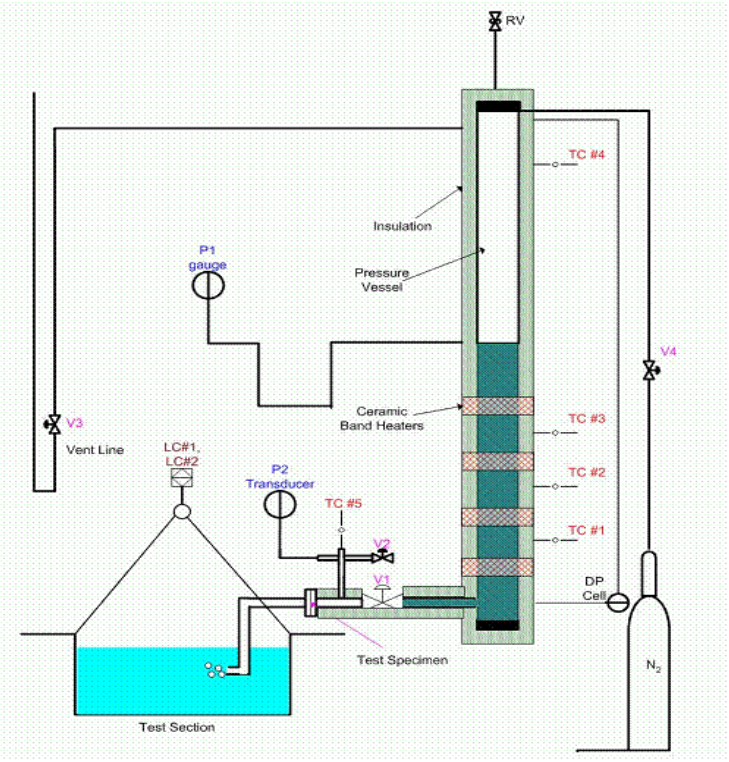

Figure 1. Schematic of test facility with measurement locations and types

2.4. Temperature Measurement

Temperatures were measured using 5 K-type stainless steel sheathed thermocouples at locations T1-T5. Measurements were taken at a rate of 1 Hz. At TC5 a tee was used to allow both pressure and temperature to be measured at the same location just upstream of the test section break. All thermocouples were inserted to the centreline of the flow at their respective locations.

2.5. Leak Rate Measurement

A 25.4 cm bolted bonnet full port gate valve initiates the experiment and the steam produced in the test section break is piped to the weigh tank where it is condensed. This allows for the dynamic measurement of the mass of water in the weigh

tank. The following describes the components involved in this measurement.

A 189.3 litre condensing tank is suspended from two high precision miniature load cells via steel cable at LC1 and LC2. The load cells work in both tension and compression and have a load capacity of 136.07 kg each. Both were manufacturer calibrated and in-house calibrated. Their full scale output is different for each, but is approximately 2.2 mV/V with a combined error of less than 0.1%. Over a 20 minute period their full scale creep is less than 0.05%. In order to increase the accuracy of the load cell data acquisition, a signal amplifier is used to amplify the signal before being recorded. All electronic components are allowed to warm up a sufficient amount of time before an experiment was conducted.

2.6. Data Acquisition

Two separate data acquisition boards made by Measurement Computing® were used for data acquisition. A PCI-DAS-TC board was used for thermocouple measurement. This board allows for 16 differential thermocouple input channels, with a resolution of 0.03 degrees C. The other board was used for the pressure transmitter, load cells, and differential pressure transducer. This board, a PCIM-DAS16JR/16 can handle up to 16 single ended or 8 differential analog inputs with 16 bit resolution. All data acquisition was streamed through and collected using a program written in Lab VIEW® software. Thermocouple data was taken at 1 Hz while all other data was taken at 20 Hz.

3. Test Samples

For obvious reasons, there are a limited number of actual steam generator tube cracks that are available for use in any experimental program. Cracked tubes that are removed from service have been studied by a limited number of groups [5, 10, 11]. These limited studies however use destructive examination and experimental techniques to establish modes of failure for the tubes with flaws. Actual tube flaws can vary in size (microscopic to macroscopic), shape, location, and roughness depending on the flaw type and morphology while in service. The flaws themselves are affected by the length of time they are in service, corrosion, vibrations and stress, as well as thermal-hydraulic conditions. This makes it difficult to study actual tube flaws in a laboratory environment, where many tests can be conducted under well controlled conditions. It is very difficult to reproduce crack-like flaws whether they are very tight, deep, corrosion, or pitting type. It is very important and advantageous however to study leak rates in well controlled environment with a well characterized crack geometry as crack opening area plays an important role in flow rates. The test samples produced in this study represent partially opened relatively large pitting flaws and axial cracks. They are machined using advanced tools which are near the lower limit of sizes capable of being produced without chemical etching techniques. This allows for precise flaw characterization.

Two types of test specimens were used in the experimental program. One is a round hole and the other is rectangular slit. The hole was drilled using a micro drill bit and the slits were laser cut by machine on 316 SS plates of thickness 3.175 mm. The drilled hole is orifice like and represents a pitting type flaw, while the laser cut slits are representative of an axial stress corrosion crack that is partially opened. The orifice hole can be seen in Figure 2. The average hole diameter was estimated as 475.5 micrometers (μm). The roughness was also estimated by measuring the valleys and peaks at the wall, and is estimated at 25 μm. The slit test specimens are numbered 2, 3, 4, 5, and 6 and increase in width respectively. Slit test specimen 2 is shown in Figure 3. As mentioned before, the slits were cut by laser. This technique cannot produce a uniform cross section through the depth of the cut due to melting effects in the material. Therefore, one side of the cut will have a slightly different area than the other. For completeness, the laser cut slit is shown with the measure slit dimensions indicated on the figure. The effective cross sectional flow area was calculated by averaging the front and back cross sections of the slits.

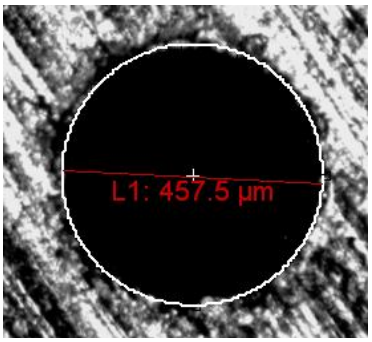

Figure 2. Pin hole crack test specimen #1.

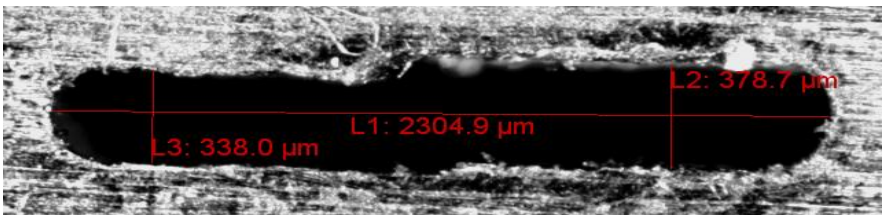

Figure 3. Slit crack test specimen #2.

4. Test Results

4.1. Cold Water Discharge Tests

Flow discharge tests were carried out with water at room temperature (20 ^{o}C). Since the water is discharged to atmospheric pressure, the upstream pressure represents total pressure drop across the slit. Using the flow rate data the Reynolds number Re, and the discharge coefficient C_d for the slit is calculated as

$$\mathrm{Re} = \frac{GD}{\mu} \tag{1}$$

$$C_d = \frac{G}{\sqrt{2\rho\Delta P}} \tag{2}$$

where, G is mass flux, D is slit hydraulic diameter, ρ is the fluid density and μ is viscosity. The data on discharge coefficient as function of pressure showed that a square-root fit to the pressure showing that in both cases the mass flux increases as a square root of pressure. The discharge coefficient for pinhole #1 varied from 0.45 to 0.48, for slit #2 it varies from 0.71 to 0.75 and for slit #6 it varies from 0.57 to 0.83.

4.2. Subcooled Flashing Discharge Tests

Test of flashing choking flow with heated water were carried out up to a vessel pressure of 6.8 MPa. Subcooling for the tests carried out varied from 25 to 50 ^{o}C. A comparison between cold water discharge tests and heated tests for slit #2 can be seen in Figure 5. Subcooling for the tests carried out on slit #2 varied from 15 to 29 ^{o}C. Data for measured discharge rate for slit #6 at four different subcoolings near the same pressure can be seen in Figure 6. This allows for the dependence of mass discharge rate on subcooling to be examined. The variance of pressure for these runs was less than 0.08 MPa. In Figure 7, the choking mass flux is shown as function of different subcooling for all slits. The choking mass flux increases as subcooling increases as expected due to a lower rate of vaporization at the test section exit. Also as the slit size increases the choking mass increases.

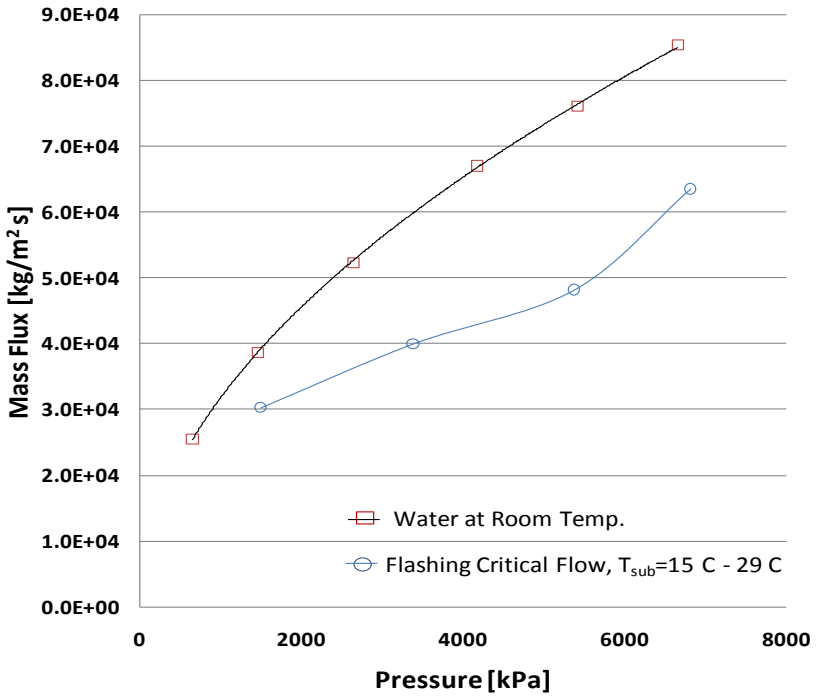

Figure 5. Cold water discharge mass flux and subcooled flashing mass flux for slit # 2

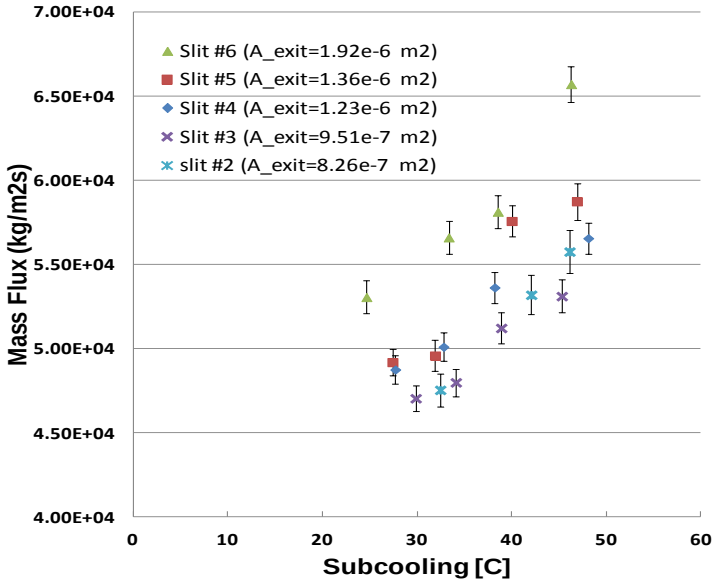

Figure 6. Choking flow in slit geometry for 7MPa tests.

4.3. Experimental Uncertainty Analysis

Experimental data uncertainty analysis was carried out for measured data such as, diameter, pressure temperatures, and mass using instrument measurement uncertainties and for the uncertainties in calculated parameters such as mass flux, error propagation method was employed. The total relative error in the mass flux data using the weight tank measurement method ranged from 1.17 % to 1.95 % for all experimental runs. Errors for a representative case are shown in Table 1. The error contributions from the different parameters of interest for the same run are shown in Table.2.

Table 1. Error for a representative test case, P = 6.7277 MPa, G=6.5707x10^4 kg/m^{2}s

Parameter	Value (1)	Standard Error (2)	Relative Error (2)/(1)
Mass flux G (kg/m2s)	65707.5	1279.3	0.01947
Pressure P (Pa)	6727738	67277.38	0.01
Temperature T (^{o}C)	237.04	1	0.0042

Table 2. Error Contribution for a representative test case

Parameter	Standard Error	Error Contribution		
Mass flux G, (kg/m2s)	1279.3	Mass 1 (kg)	Mass 2 (kg)	Area (m2)
		456.627	465.627	314.572

5. Choking Flow Model for Slits

A one-dimensional model for two-phase choking flow was developed. A reservoir contains a fluid at constant pressure P_0 and temperature T_0 called the stagnation state. If the back pressure P_b is equal to P_0 then obviously no flow will occur in the channel. As P_b decreases, flow begins and a pressure gradient is established along the channel. Also, as P_b decreases, the flow rate increases until the back pressure reaches a critical pressure. At this point choking flow is obtained and any reduction in P_b beyond P_c does not change the flow rate or the pressure gradient in the channel. If the stagnation state is at saturation, then the entrance loss of the channel will cause the fluid to flash at the entrance. In this case, the channel only contains a two-phase mixture. In the case of higher subcooling, flashing will occur somewhere along the length of the channel. If one considers flashing to begin when the fluid reaches saturation, then flashing will occur at the point along the channel where the pressure drops below the corresponding saturation pressure at the stagnation temperature T_0. This is consistent with a homogeneous equilibrium model. This pressure drop is attributed to the single phase liquid frictional pressure drop along the channel. It is well known however that some amount of liquid superheat is required to produce and maintain vapour generation. With these considerations, a homogeneous equilibrium mode (HEM) is developed as well as a

homogeneous nonequilibrium model (HNEM).

In case of HNEM for non-equilibrium effects to take place, the liquid must become superheated to allow for vapour generation. Alamgir and Lienhard [11] proposed a model for flashing inception based on pressure undershoot. They found that the liquid phase depressurizes below the saturation value, corresponding to the superheat required for vapour generation. Figure 7 show a comparison of the model predictions with SG simulated tube data of Revankar et al. [12] and channel length of 3.17mm. Again for the case of subcooled stagnation conditions and for much smaller channel length the HE model under predicts the critical mass flux data by as much as 27%. Again however, the HNEM model better predicts the data and is accurate to within 11% for the cases presented here.

6. Conclusions

The ability to estimate the leak rates from the through-wall cracks in the steam generator tube is important in terms of radiological source terms and overall operational management of steam generators. A literature survey showed that there are few data sets available on crack geometries related to steam generator tubing. An experimental program was carried out measuring subcooled flashing flow rate through well defined simulated crack geometries with L/D<5.5. As subcooling increases the flashing discharge rate also increases. A homogeneous non-equilibrium model for flashing flow in steam generator tube crack was modelled. The prediction from HENM agreed well within 10% of experimental data for choking discharge rates from such geometries.

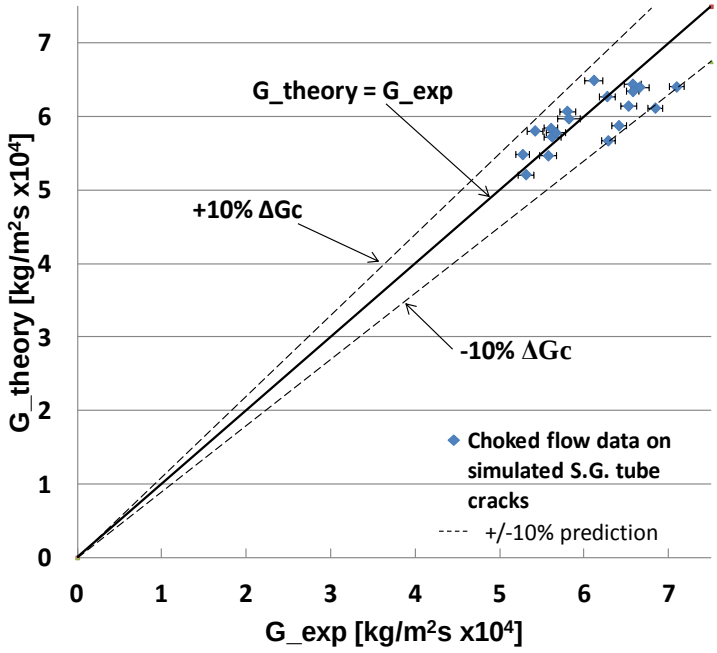

Figure 7. Comparison of HENM with experimental data

Acknowledgements

The work was partly supported by Canadian Nuclear Safety Commission. One of the authors (STR) was partially supported by World Class University program through the National Research Foundation of Korea funded by the Ministry of Education, Science and Technology (R31-30005).

References

[1] Majumdar, S., 1999, Prediction of structural integrity of steam generator tubes under severe accident conditions, Nuclear Engineering Design, 194, p. 31.

[2] Vaia, A. R., Stevens, J. M., Prabhu, P. J., 2005, "Laboratory examination of pulled steam generator tube with free span axial ODSCC," 12th International Conference On Environmental Degradation of Materials in Nuclear Power Systems, Salt Lake City, Utah, Minerals, Metals and Materials Society, pp. 1113-1123.
[3] Fuller, E., 2006, Steam Generator Integrity Assessment Guidelines Revision 2 Non-Proprietary Version1012987, Final Report. EPRI Technical Report TR-1012987.
[4] Keating, R. F., Hernalsteen, P., Begley J. A., 1955, Burst pressure correlation for steam generator tubes with throughwall axial cracks. Electric Power Research Institute, Palo Alto, California, EPRI Technical Report TR-105505.
[5] Kuchirka , et al., 1997, Oconee 2 Steam Generator Tube Examination, EPRI Technical Report TR-106863.
[6] Henry, R.E., Fauske, H. K., 1970, Two-phase critical flow at low qualities, Part I: experimental; Part II Analysis. Nuclear Science and Engineering, 41, p. 89.
[7] Henry, R.E., Fauske, H. K., 1971, The two-phase critical flow of one-component mixtures in nozzles, orifices, and short tubes. Journal of Heat Transfer, 93, p. 179.
[8] Henry, R. E., et al., 1975, Heat Transfer at Low Temperature, Plenum Press, New York, Ch.11.
[9] Pagan, S,, Duan, X., Kozluk, M. K., Mills, B., Goszczynski, G., 2009, Characterization and structural integrity tests of ex-service steam generator tubes at Ontario Power Generation. Nuclear Engineering Design, 223, p. 477.
[10] Westinghouse Electric Corporation, 1977, Burst Pressure correlation for steam generator tubes with through-wall axial cracks. EPRI, Palo Alto, Report, EPRI TR-105505.
[11] Alamgir, M., Lienhard J.H., 1981, Correlation of pressure undershoot during hot water depressurization. ASME Journal of Heat Transfer, 103, p. 52.
[12] Revankar, S. T., Wolf, B., 2010, Probabilistic assessment of leak rates through steam generator tubes. Final Report to Canadian Nuclear Safety Commission, PU/NE-10-06.

Available online at www.sciencedirect.com

SciVerse ScienceDirect

Procedia Engineering 00 (2012) 000–000

Procedia Engineering

www.elsevier.com/locate/procedia

5th BSME International Conference on Thermal Engineering

Both experimental and numerical investigation on breakup length of cylindrical falling jet

Raihan Tayeb[a]*, Md. Nazmus Sakib[a], Mohammad Ali[a], M. Quamrul Islam[a]

[a]*Department of Mechanical Engineering, Bangladesh University of Engineering and Technology (BUET), Dhaka 1000, Bangladesh*

Abstract

The variation in breakup length of a liquid jet subjected to different physical parameters is investigated experimentally. The different parameters are jet velocity, Reynolds number and Weber number. Effect of gravity on breakup length is also studied. Jet breakup process is simulated numerically by solving the transient axisymmetric equations of continuity and motion using an algorithm based on the Volume of Fluid (VOF) method that was previously proven successful in simulations of steady-state liquid jets. The experimental results are compared with the numerical simulation and discrepancies are discussed. The experiment shows that the breakup length first decreases with the increase of jet velocity and then increases with much higher velocity. The simulation result shows the expected pattern of the jet breakup process with satellite drop formation and droplet oscillation as can be found in experiment. It also shows the transient variation in the jet breakup process.

Keywords: Jet breakup; breakup length; volume of fluid.

1. Introduction

Liquid jet breakup process has been the subject of interest for over a century. Studies on the liquid jet breakup process have led to many practical applications like inkjet printing, liquid jet propulsion system, spraying and coating system. Notable applications are emerging in the field of micro and nanofluidics. Modern printers are using microfluidic inkjet devices for high speed and precise color printing. Thus the importance of understanding the phenomenon of jet breakup and drop formation has greatly increased. The variation of liquid jet breakup length with jet velocity and other parameters was experimentally studied by many scientists like Haenlein , 1932, Grant and Middleman, 1966, McCarthy and Malloy,1974 and Hirosyasu et al, 1991. They studied the shape of the breakup curve and discussed the effects of ambient gas and fluid properties on breakup length.

Numerical investigation of the jet breakup process poses a challenging problem since a numerical method in this case must have the capability to track large deformation of free surfaces as well as disintegration of liquid into droplets. However, the arrivals of new numerical methods and large increase in computing power have made the use of computational fluid dynamics (CFD) a viable means of simulating the liquid jet breakup process. Schulkes, 1994 and Zhang and Stone, 1997, for example, have studied the formation of two - dimensional, axisymmetric droplets using the boundary element method. Gueyffier et al, 1999 used volume of fluid interface tracking method and piecewise linear scheme to simulate liquid flow problem. Richards et al., 1995 have also studied liquid jet formation from a nozzle in to a second

* Corresponding author. Tel.: +880-1814827204.
E-mail address: raihanme06@yahoo.com

liquid using a volume of fluid (VOF) approach. Wilkes et al, 1999 solved the full, axisymmetric Navier–Stokes equations for the formation of a drop of Newtonian liquid at the finite Reynolds numbers using the finite element method.

Although a wide variety of numerical methods are now being applied to the problem of drop formation, VOF remains the most commonly used method for simulating liquid jet and drop formation. It has been successfully used to capture fine flow details such as satellite drop formation. Renardy and Renardy, 2002 used a parabolic reconstruction of surface tension for VOF method and showed that numerical difficulties encountered at the free surface for surface tension dominated flows may be avoided.

In recent years jet breakup has been studied extensively using high speed digital cinematography. Researchers tried to find the relationship between jet breakup, Reynolds number, Weber number, wave length of perturbation and temperature. The objectives of the present study are to use the VOF based numerical method for calculating liquid-gas jet dynamics, from the start-up of their time evolution to their apparent steady-state involving the region from the nozzle exit to their breakup through necking and detachment of drops. Our aim is to predict the jet length and the shape, as well as their relationship with jet velocity. The experimental data and comparisons reported here fill the gaps in viscosity and flow rate not considered in previous studies.

2. Experimental Setup

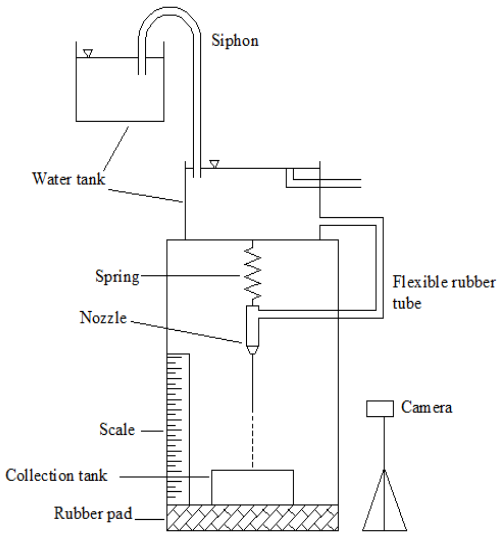

Fig 1: Schematic of the experimental arrangement

The setup consists of a reservoir of water with arrangement to maintain constant water level, a nozzle to produce a vertical jet directed toward the collection bucket and a transparent plastic scale attached aside the jet to measure the breakup length and droplet size. The constant water level is maintained using a siphon, that transfers water to the reservoir from another reservoir and the excess water is released with an overflow pipe set at a certain height of the reservoir. The diameter of the jet is 4 mm. The droplet diameters are measured from photographs by image processing. Photographs are taken with a digital camera. A digital balance is used to measure the weight of the water collected in the collection reservoir. There were arrangements to keep the whole setup dark except the jet to get good and clear photographs. The disintegration of liquid jet is very much sensitive to the vibration of the floor. To eliminate the vibration water is transferred from the reservoir to the nozzle through a soft hose and the transfer hose and the nozzle is suspended through a soft spring. The base of the experimental frame was covered with rubber pad to damp out the vibration that transferred from the floor to the nozzle.

3. Mathematical modeling

The flow in each phase is considered axisymmetric, viscous (Newtonian), and incompressible. The continuity equation is given in cylindrical, axisymmetric coordinates (r, z) as:

$$\frac{\partial u}{\partial r}+\frac{\partial v}{\partial z}+\frac{u}{r}=0 \tag{1}$$

Where u and v are the radial and axial components of the velocity field, respectively. The Navier-Stokes equation is given as:

$$\rho\left(\frac{\partial u}{\partial t}+u\frac{\partial u}{\partial r}+v\frac{\partial u}{\partial z}\right)=-\frac{\partial p}{\partial r}+\frac{\partial \tau_{rr}}{\partial r}+\frac{\partial \tau_{zr}}{\partial z}+\frac{\tau_{rr}}{r}+\sigma\kappa f n_r \tag{2}$$

$$\rho\left(\frac{\partial v}{\partial t}+u\frac{\partial v}{\partial r}+v\frac{\partial v}{\partial z}\right)=-\frac{\partial p}{\partial z}+\frac{\partial \tau_{rz}}{\partial r}+\frac{\partial \tau_{zz}}{\partial z}+\frac{\tau_{rz}}{z}+\rho g n_z+\sigma\kappa f n_z \tag{3}$$

Where,

$$\tau_{rr}=2\mu\left(\frac{\partial u}{\partial r}\right)$$
$$\tau_{zr}=\tau_{rz}=\mu\left(\frac{\partial v}{\partial r}+\frac{\partial u}{\partial z}\right)$$
$$\tau_{zz}=2\mu\left(\frac{\partial v}{\partial z}\right)$$

Where ρ is the density, p the pressure, μ the viscosity, σ the surface tension, κ the curvature of surface, n the unit normal to the surface and f is a function for continuous change of the color variable (here density) across the thickness of fluid interface.

For numerical simulation, volume of fluid (VOF) method based on a simplified treatment of the Navier-Stokes equations with a fixed, regular, uniform grid is used to solve the problem. Geometric Reconstruction Scheme (piecewise-linear) is implemented for the advection of the liquid interface. The treatment of surface tension consists of artificially smoothing the discontinuity present at the interface in a Continuum Surface Force (CSF) manner.

4. Results and Discussion

4.1 Breakup length as a function of velocity

Breakup length obtained from the experiment is plotted against jet velocity and is shown in Fig 2. It shows that as the jet changes from laminar to turbulent the breakup length drops and then starts increasing. This is agreement with previous studies on jet breakup length. Previous studies on jet breakup length have shown that there are actually four breakup regimes. These are Rayleigh regime, the first wind-induced regime, the second wind-induced regime,and the turbulent atomization regime (Reitz & Bracco, 1999). The breakup length curve in our case shows only the second wind-induced regime and the turbulent regime. However beyond the first wind-induced breakup regime there is confusion about the breakup length trends. For example, Haenlein reported that the jet breakup length increases again with increasing jet velocity, and then abruptly reduces to zero. McCarthy & Malloy reported that the breakup length continually increases. More recently, Hiroyasu et al discovered discontinuous elongations and shortenings of the jet with changes in the jet velocity. These apparent anomalies are associated with changes in the nozzle internal flow patterns caused by separation and cavitation phenomena. Jets from cavitating nozzles were found to have very short breakup lengths. Detached flow jets have long breakup lengths.

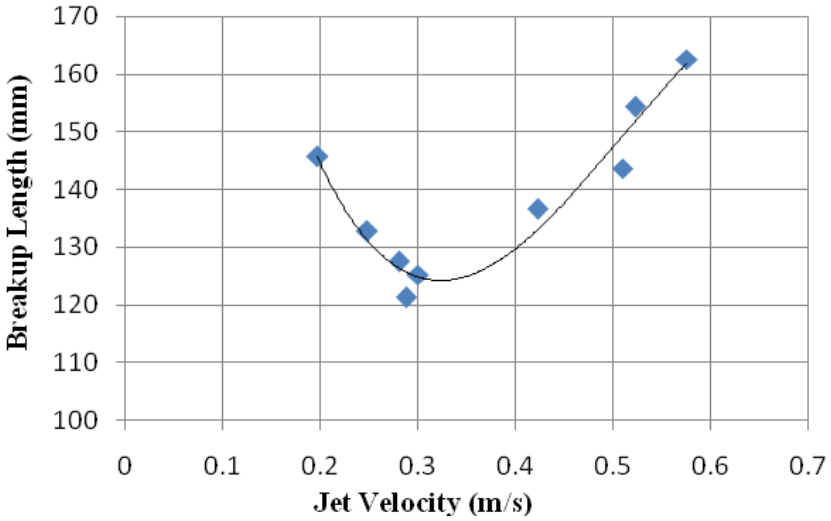

Fig 2: Breakup length against jet velocity

To find the effect of gravity the dimensionless breakup length found from the experimental and numerical results is plotted in a log graph against jet velocity and compared with the experimental work of Grant and Middleman. Grant and Middleman experimented with jet velocity at gravity less condition and gave a correlation. The Grant-Middleman's correlation is as follows

$$\text{Laminar: } L/d = 19.5\,(We^{1/2} + 3We/Re)^{0.85} \quad (4)$$

$$\text{Turbulence: } L/d = 8.51\,(We^{1/2})^{0.64} \quad (5)$$

Where L is the jet breakup length, d the nozzle width, We the Weber number ($We= \rho v^2 d/ \sigma$) and Re the Reynolds number ($Re= \rho v d/ \mu$). If the experimental and numerical breakup length curve is compared with the data of Grant-Middleman which is obtained in gravityless condition it is found that gravity has the effect of reducing breakup length. This is reasonable since gravity accelerates the liquid column and reduces its diameter.

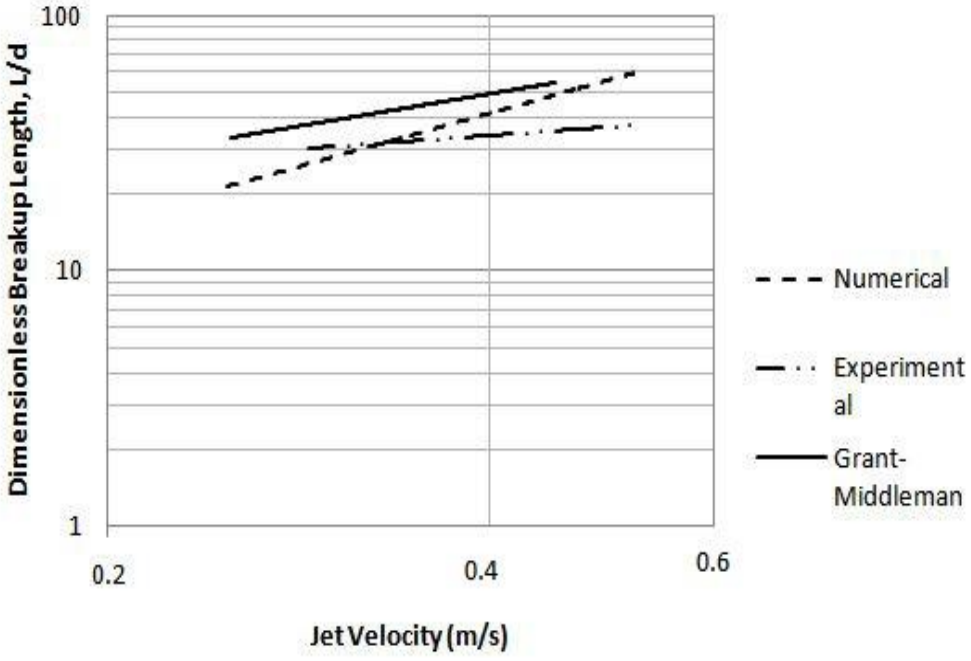

Fig 3: Breakup length as a function of jet velocity (log- log plot)

4.2 Transient variation of breakup length

Variation of breakup length with time for different jet velocities is obtained from the numerical simulation of jet breakup. The results are shown in the following graphs for jet velocities 0.248 m/s, 0.3 m/s and 0.423 m/s.

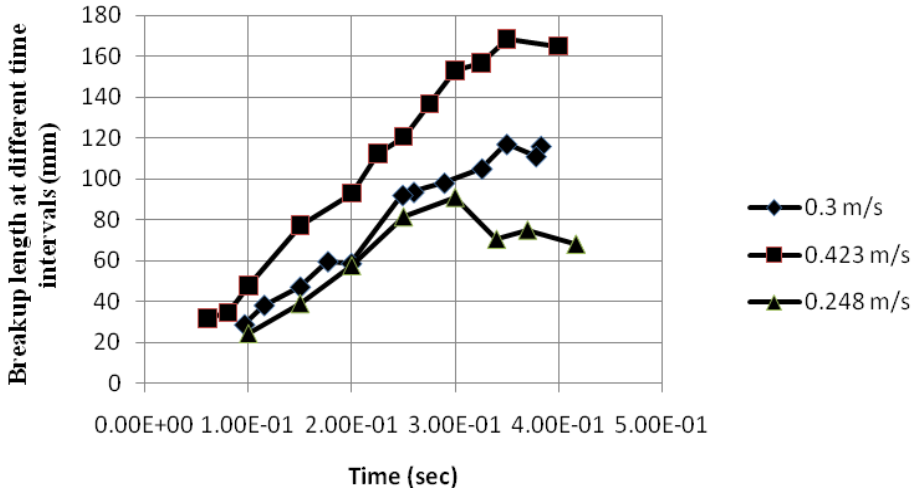

Fig 4: Breakup lengths at different time intervals

The graphs show that breakup length at first increases quite rapidly, reaches a maximum and then oscillates about a mean length. The oscillation occurs because when a droplet is detached from the main liquid column, the column recoils before a second droplet starts forming. Fig 5 show how breakup length changes over time for velocity of 0.248 m/s

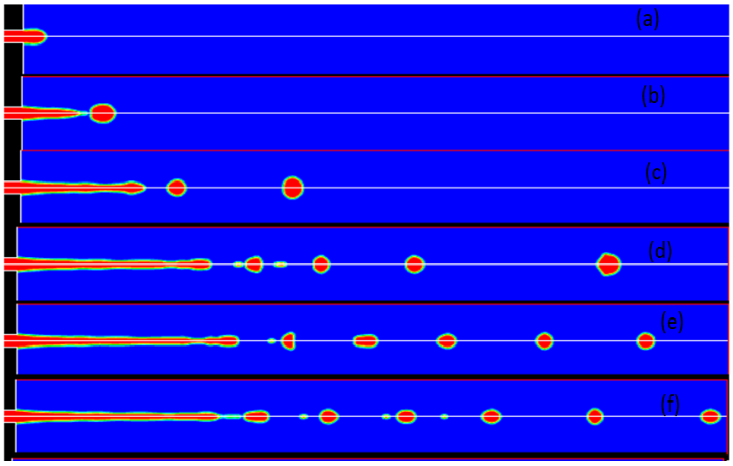

Fig 5: Result of simulation for flow velocity 0.248 m/s at times (a) 0.03 sec, (b) 0.09 sec, (c) 0.15 sec, (d) 0.21 sec, (e) 0.27 sec, (f) 0.33 sec.

5. Conclusion

Experimental investigation of the variation of breakup length of liquid jet with changing jet velocity is found to agree well with the work of other experimenters. The breakup curve obtained shows two breakup regimes - the second wind-induced regime and the turbulent regime. By comparing the experimental and numerical breakup curve with the data of Grant-Middleman it is found that gravity has the effect of reducing breakup length. This is reasonable since gravity accelerates the liquid column and reduces its diameter. However slight discrepencies are seen between the numerical curve and experimental curve. The former gives larger breakup length than the experimental one. This may be due to the presence of external perturbation which is always present during the experiment and which is very difficult to eleminate. This external perturbation instigates the breakup process and causes shorter breakup length which is why our experimental curve is below the numerical curve. However at low jet velocities adhesion of liquid with the nozzle may results in increased breakup length in the experiment. Transient variation of breakup length is also obtained from the numerical results. The results show that breakup length at first increases quite rapidly, reaches a maximum and then oscillates about a mean length. The

oscillation occurs because when a droplet is detached from the main liquid column, the column recoils before a second droplet starts forming.

References

[1] Haenlein, A., 1931. Disintegration of a liquid jet. NACA-TM-659 (1931).

[2] R. P. Grant, S. Middleman, 1966. Newtonian jet stability, AIChE J., 12, 669–677.

[3] McCarthy, M. J., and N. A. Malloy, 1974. Review of stability of liquid jets and the influence of nozzle design. Chem. Eng. J. 7, 1.

[4] Hiroyasu H, Arai M, Shimizu M. 1991. Breakup length of a liquid jet and internal flow in a nozzle. Proc. ICLASS-91, Pap. 26.

[5] Schulkes, R.M. ., 1994. The evolution and bifurcation of a pendant drop. J.Fluid Mech, 278,83–100.

[6] Zhang, D.F. and Stone, H.A. Drop formation in viscous flows at a vertical capillary tube. Phys.Fluids, 1997, 9(8), 2234–2242.

[7] D.Gueyffier, J.Li,A.Nadim, R.Scardovelli, S.Zaleski, 1999. Volume-of-fluid interface tracking with smoothed surface stress methods for three-dimensional flows, J. Comput.Phys.152, 423–456.

[8] Richards, J.R., Beris, A.N., and Lenhoff, A.M.,1995. Drop formation in liquid–liquid systems before and after jetting. Phys.Fluids, 7(11),2617–2630.

[9] Wilkes, E.D., Phillips, S.D., and Basaran, O.A., 1999.Computational and experimental analysis of dynamics of drop formation. Phys.Fluids, 11(12), 3577–3598.

[10] Renardy, Y. and Renardy, M., 2002. PROST: a parabolic reconstruction of surface tension for the volume-of fluid method. J.Comput.Phys., 183,400–421.

Available online at www.sciencedirect.com

SciVerse ScienceDirect

Procedia Engineering 00 (2012) 000–000

Procedia Engineering

www.elsevier.com/locate/procedia

5th BSME International Conference on Thermal Engineering

Visualisation of Air Entrainment by a Plunging Jet

A. K. Roy[a], B. Maiti[b,*] and P.K. Das[b]

[a]*Department of Mechanical Engineering, BIT Mesra, Ranchi, 835215, India*

[b]*Department of Mechanical Engineering, IIT Kharagpur, Kharagpur, 721302, India*

Abstract

The phenomenon of air entrainment by water jet plunging on the free surface of a water pool is reported in the paper. An effort has been made to understand the physics of the phenomenon through elaborate visual and photographic observations. The formation of air sheath, the downward motion of the two phase jet, the reversal of the jet motion has been reported. The visualisation of the random motion of a single bubble has also been reported.

Keywords: Air entrainment, plunging jet, flow visualisation

Nomenclature

d_N	diameter of the nozzle, mm
L_N	length of the nozzle, mm
V_C	critical velocity, m/s
Z	vertical distance, mm
H_N	height of nozzle from free surface of water, mm
r	radius, mm
V_N	jet velocity at the exit of the nozzle, m/s

1. Introduction

Air entrainment due to plunging liquid jets and consequently both bounded and unbounded air water two-phase flow can be observed in nature and in many industrial situations. A plunging liquid jet is defined as a moving column of liquid that passes through a gaseous headspace before impinging on the free surface of receiving liquid pool.

The mechanism of air entrainment due to plunging liquid jets is very complex and the complete mechanism of air entrainment is not fully understood till date. Due to liquid jet impingement on a free surface of liquid, a depression on the meniscus is formed at low jet velocity. Further increase in liquid jet velocity cause an air sheath or envelop formation on the periphery of the liquid jet just below the free surface of liquid. The air sheath is unstable in nature. The make and collapse of the air sheath induces formation of air bubbles below the liquid surface; thereby atmospheric air is entrained in the liquid body. Here below the liquid surface a downward biphasic cone is formed. The entrained air bubbles reach up to a certain

* Corresponding author. Tel.: +91-3222-277536; fax: +91-3222-255303.
E-mail address: bmaiti@mech.iitkgp.ernet.in

depth below the liquid surface, and then start rising in the upward direction in a helical path. The upward rising bubbles form a concentric envelop around the downward biphasic cone.

Air entrainment due to plunging liquid jets can be exploited for a number of advantages. For example, to achieve good absorption coupled with good mixing in some gas-liquid reactors, plunging jet aeration provides a very simple and effective way of dissolving air in the reactors. To achieve adequate aeration, many biological processes use spargers or airlift fermenters apart from jet aeration. In wastewater treatment, plunging jet aeration is more advantageous as compared to airlift fermenters when the reactor media is highly viscous due to presence of heavy sludge of organic matter. Due to simplicity in construction and relatively less operational difficulties, the jet aerators have potential application in many chemical fermentation and floatation processes.

In the natural process of self-purification of rivers, streams, waterfalls and weirs, undoubtedly, jets that entrain air and provide good contact and dispersion of air bubbles into the body of water play a very significant role. In the Oceans, plunging breaking waves can entrain a large amount of air bubbles when the top of the wave forms a water jet projecting ahead of the wave face and impacts the water free surface in front of the wave.

Before 1970, there were only a few serious attempts made to study the phenomena of air entrainment by plunging liquid jets. Since then, the interest and the scope of the experimental study on plunging liquid jet systems have increased. One of the first scientific accounts in this regard was made by Leonardo Da Vinci (AD 1452-1519).

Bin and Smith (1982) presented some reviews on various aspects of plunging liquid jet system. More general reviews on plunging liquid jet systems, including classifications; their description and applications are found in Bin (1993). The studies and observations by Cummings and Chanson (1999) show that air entrainment due to plunging jets takes place when the liquid jet impact velocity exceeds a certain characteristic velocity which is a function of inflow conditions.

Robertson et al. (1973) observed that the formation of a stable air sheath around the jet depends on the ambient pressure. Michel (1984) observed that the air sheath behaves as a ventilated cavity. The length of the air sheath fluctuates considerably and air pockets are entrained by discontinuous ‘gusts’ at the lower end of air sheath. Kusabiraki et al. (1990) measured the length of the air sheath using high-speed photographic technique. They have found that the length of the air sheath increases with the increase in liquid jet velocity.

McKeogh and Ervine (1981) classified the mechanism of air entrainment as (i) annular oscillations; (ii) intermittent vortex; (iii) turbulent occlusion and (iv) droplet entrainment. Davoust et al. (2002) identified the air entrainment process due to plunging liquid jet as the consequence of two complementary mechanisms: (a) the interfacial shear along the liquid jet interface which drags down an air boundary layer and (b) the entrapment process at the point of impact of the plunging jet with the receiving pool. The latter process is usually dominated by growing interfacial disturbances traveling on the jet.

El Hummoumi et al. (2002) studied the inception condition for different range of Reynolds number and Weber number of liquid jet and presented the thresholds for air entrainment.

Chanson et al. (2002, 2004) performed experimental study on basic entrainment characteristics in air-water plunging liquid jet system for a wide range of flow situations and found the lowest inception velocity as 0.73 m/s in the entire range of their experimental condition. They observed that for liquid jet velocities slightly greater than the inception velocity, entrainment of individual air bubbles occur, but at the larger speeds air cavity develops all around the perimeter of the jet and most of the air is entrained by elongation, stretching and breakup of the ventilated cavity. They have performed the experiment for three scale models based on an identical Froude number. For jet velocities slightly greater than inception velocity, the entrained air bubbles having sizes of around 0.5 – 1 mm and for larger jet velocities the sizes of the entrained bubbles in the developing flow region are in the range of 0.5 – 5 mm as observed by them.

A common observation of the above and many other researchers on the air entrainment in a plunging liquid jet system is that it mainly depends on some primary variables like jet diameter, jet velocity, jet length and physical properties of the fluid. Literatures indicate that most of the investigations on plunging liquid jet are through experiments. However, the observations made in different investigations are not identical. This leaves a scope for further experiments.

2. Experimentation

The experimental setup fabricated for the present study, shown in Fig. 1, consists of following major components.

(1) Transparent Acrylic Tank: The tank is fabricated from 10 mm transparent acrylic sheets. The dimension of the tank is 1500 mm in length, 750 mm in width and 750 mm in height. Near the bottom of the side vertical faces two 20 mm openings are provided. This ensures symmetric suction draw out pattern with respect to tank mid zone. These two openings are connected to the suction side of a centrifugal pump. This facilitates circulation of water in the experimental system.

(2) The nozzle for jet impingement: For the purpose of jet impingement on the surface of water in the tank, two different nozzles are used. The inner diameters of the nozzles are 4 mm and 6 mm respectively. The length of those nozzles is kept constant and is 200 mm. The nozzles are made of copper with nickel coating on it. The nozzle is feed with water from the delivery of centrifugal pump mentioned earlier. A pre-calibrated orifice meter fitted in line measures the flow rate through the nozzle. Thus the suction tubes from the tank to the pump and delivery into the tank through orifice meter and nozzle create a closed loop system.

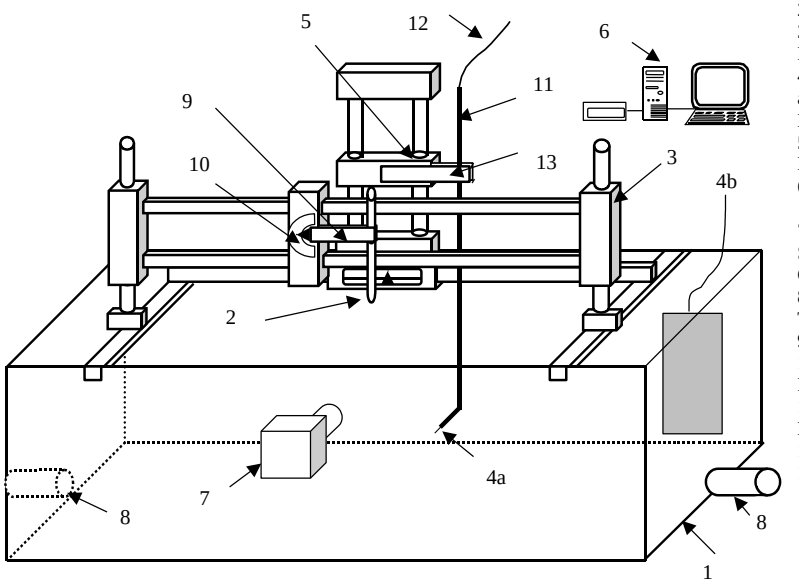

Fig. 1 Water jet impingement apparatus

(3) Traversing mechanism for the nozzle: For the purpose of the experimentation, the location of the nozzle outlet can be varied through a traversing mechanism on to which the nozzle is attached. Through sliding arrangements the nozzle can be traversed along the length and along the width of the tank on a horizontal plane. Graduated scales placed on the traversing mechanism can measure the position of the nozzle in the horizontal plane. The nozzle can also move in the vertical direction so that the distance between the nozzle outlet and water surface can be varied. Moreover, with respect to a horizontal axis the nozzle can rotate in a vertical plane.

(4) Flow visualization system: A digital camera (SONY DSC-F717, Sony Electronics Inc. NJ, image device–11mm (2/3 type), CCD primary color filter, with approximately 5240000/5020000 pixels, lens with focal length of 9.7- 48.5 mm, and more precisely 38 - 190 mm when converted to a 35 mm still camera) is used in still and video mode with proper lighting arrangement to visualise the nature of the two-phase flow. The images were analyzed frame wise to visualise the geometry of the biphasic zone and to understand two-phase flow phenomenon due to liquid jet impingement.

2.1. Experimental Procedure

The acrylic tank is filled with water from a domestic water purification plant supply up to a pre-determined height. The pump is made operational which receives water from the tank and discharges into the water surface through the nozzle. The amount of water supply is monitored and the flow rate through the nozzle is controlled with the help of two valves fitted in

the pump bypass and delivery line respectively. The temperature of the water in the tank is monitored with a thermometer. During experimentation, whenever the temperature of water raised by approximately 2^0C, the experimentation was discontinued till the water temperature falls back to initial temperature. The range experimentation is given in Table 1.

Table 1. The Range of Experimentation

Nozzle diameter d_N (mm)	Jet velocity v_N (m/s)	Nozzle height H_N (mm)	Nozzle geometry L_N/d_N
4	3.25 - 5.5	50, 300	25
6	2.23 - 4.18	50, 300	25

3. Results and Discussion

The phenomenon of air entrainment by a plunging liquid jet has been investigated through visual and photographic observations. For the photographic recording a digital camera, as mentioned earlier, was used with proper illumination. The visual observation is explained below.

A schematic representation of air entrainment and bubble formation below the free surface of water is shown in Fig. 2. Air entrainment is observed when the jet velocity reaches a critical (inception) velocity, below which no entrainment of air can be observed. The inception velocity for the present range of experimentation is tabulated in Table 2.

Table 2. Inception velocities (v_C)

Nozzle diameter, d_N (mm)	Nozzle height, H_N (mm)	$v_{C,}$ (m/s)
4 and 6	50	1.6
4 and 6	300	1.2

When the jet of water strikes the free surface of stagnant water at a velocity below the inception, a depression on the meniscus of the free surface of water is formed. As the jet velocity increases the depression of the meniscus also increases. Just above the inception velocity, air is entrained in the form of a limited number of individual bubbles and the entrainment is observed to be intermittent. The sizes of the entrained bubbles are visibly small and the bubbles follow a slightly helicoidal trajectory around the jet centerline. The entrained bubbles travel in the downward direction with a gradually decreasing velocity. At one point its downward velocity becomes zero and then it starts rising. Some of the bubbles succeed in reaching the free surface while the rest are caught in the pocket of downward moving liquid and continue to have a zigzag circulatory motion in the vertical plane.

As the jet velocity further increases, formation of air sheath around the periphery of the jet below the impact point is observed. Fig. 3, shows the photograph representing formation of air sheath. With further increase in jet velocity, the size of the air sheath also increases. The entrainment of air is due to make and collapse of the oscillating air sheath and the entrainment is observed to be continuous in nature. The entrained air bubbles are carried away below the free surface of water by the jet because of its momentum. Fig. 4, shows the closer view of the air sheath around the jet. Below the free surface of water, the downward (primary) air bubbles form a cluster, which resembles like a cone.

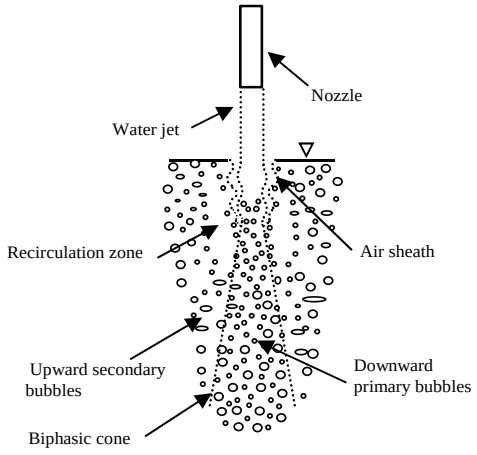

Fig. 2 Schematic representation of bubble formation due to liquid jet impingement

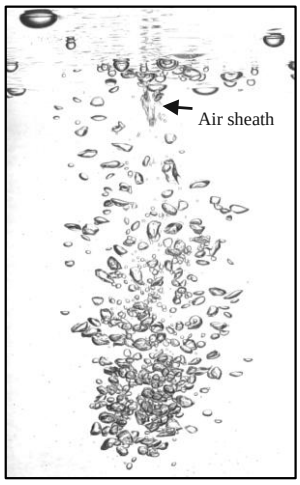

Fig. 3 Photograph showing the formation of air sheath (v_N = 2.25 m/s, d_N = 4 mm, H_N = 50 mm)

Within this biphasic cone, smaller bubbles are seen in the upper portion while at the lower portion relatively large bubbles are observed. The coalescence of air bubbles takes place at the lower portion of the cone. Hence, relatively larger bubbles are observed at the lower portion of the biphasic cone.

The downward (primary) air bubbles penetrate the water pool up to a certain depth below the free surface of water. This depth of penetration of air bubbles increases with the increase in jet velocity and decreases with the increase in height of the nozzle from the free surface of water. The smaller bubbles reach deeper below the free surface of water and stay for a longer time at that depth than the larger bubbles. When the bubbles reach the maximum depth of penetration they slow down and start rising freely towards the free surface of water in a helicoidal trajectory.

Some of the rising bubbles, which are very near to the edge of the biphasic cone, cannot simply rise up to the free surface of water and escape. These bubbles are dragged downward by the two-phase jet and form a recirculation zone near the edge of the biphasic cone. This recirculation is observed to be more vigorous at the upper portion as compared to the lower portion of the edge of the biphasic cone. The upward (secondary) bubbles form an envelope around the primary bubbles and the entire biphasic zone resembles like a cylinder with a sharpened end at the bottom as shown in Fig. 5. The visual observation of the phenomenon of air entrainment agrees with the observations by (Bin 1993, Mckeogh and Ervine 1981, Chanson et al. 2004 and other researchers).

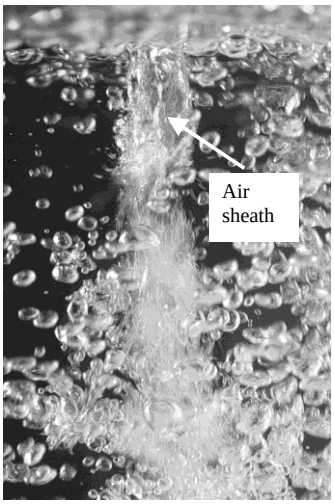

Fig. 4 Closer view of photograph of air sheath (v_N = 3.6 m/s, d_N = 6 mm, H_N = 50 mm)

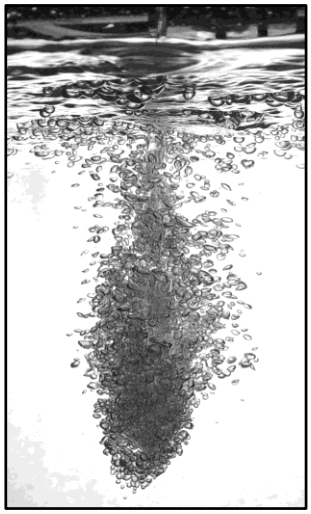

Fig. 5 Shape of the biphasic zone (v_N = 5.50 m/s, d_N = 4 mm, H_N = 300 mm)

The rise of secondary air bubbles are in the form of lumps are clearly visually observed and they are shedding alternately from the biphasic cone from diametrically opposite directions, whose photograph is shown in Fig. 6. This phenomenon of vortex formation is reported by Bonetto and Lahey Jr. (1993) but the mechanism is not well understood.

A study on the trajectory of a single bubble entrained due to liquid jet impingement in the vertical plane parallel to the jet axis is made using a digital camera. The entrainment of a single air bubble is made with some trial and error by adjusting liquid jet velocity and nozzle height. The coordinates of the single moving bubble were measured from the frame wise analysis of pictures. Smooth joining of the coordinate points at successive time intervals revealed the trajectory of a single bubble as shown in Fig.7. The trajectory shows a zigzag up and downward oscillation pattern with circular motion of the bubble around the jet axis. This random pattern of the bubbles is useful for good mixing characteristics for jet aerators. This may be one of the reasons why plunging jet aerators are extensively used for aeration and good mixing in gas-liquid reactors. The bubble reaches up to a certain depth and stays for a longer time at that depth with movement in lateral direction. The maximum radial shift of the bubble at maximum penetration depth matches with the dimension of an equivalent biphasic cone, which forms at that experimental condition.

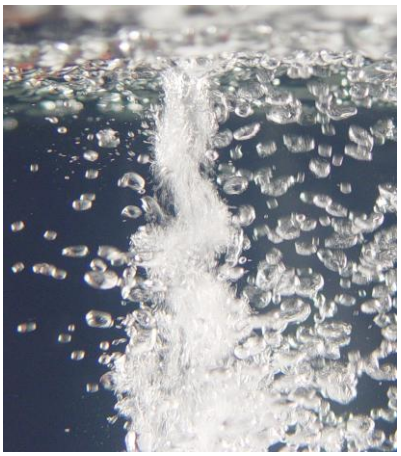

Fig. 6 Formation of vortex due to plunging jet (v_N = 3.2 m/s, d_N = 4 mm, H_N = 300 mm)

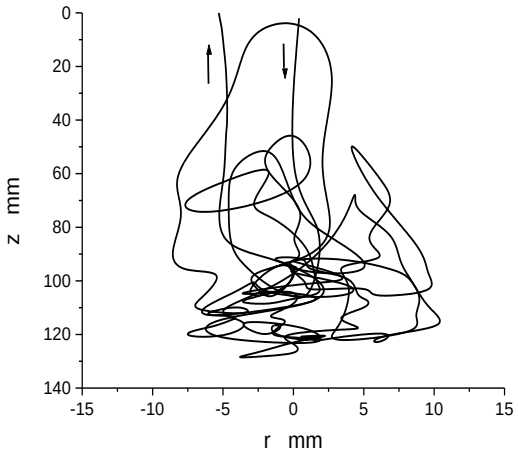

Fig. 7 Trajectory of a single entrained bubble

4. Conclusion

Air entrainment due to impingement of a water jet on the free surface of water has been investigated. A comprehensive visualisation study reveals that the inception of entrainment is due to the formation of an air sheath surrounding the jet just below the interface. This air sheath breaks into bubbles further downstream. Initially the bubbles migrate in the downward direction and grow bigger due to coalescence. The bigger bubbles then move upward and escape through the free surface. The visualization also reveals a typical vortex structure. The random bubble motion has also been captured by digital image processing from the motion of a single bubble.

References

[1] Bin, A. K., 1993, "Gas Entrainment by Plunging Liquid Jets," *Chem. Eng. Sci*., Vol. 48, pp. 3585-3630.
[2] Bin, A. K., and Smith, J. M., 1982, "Mass Transfer in Plunging Liquid Jet Absorber," *Chem. Eng. Commun*., Vol. 15, pp. 367-383.
[3] Bonetto, F., and Lahey Jr, R. T., 1993, "An Experimental Study on Air Carryunder Due to a Plunging Liquid Jet," *Int. J. Multiphase Flow*, Vol. 19, pp. 281-294.
[4] Chanson, H., Aoki, S., and Hoque, A., 2002 "Similitude of Air Entrainment at Vertical Circular Plunging Jets," *Proc. of ASME FEDSM'02, ASME 2002 Fluids Engineering Division Summer Meeting*, Montreal, Quebec, Canada, July 14-18, Paper FEDSM 2002-31024, pp.1-6.
[5] Chanson, H., Aoki, S., and Hoque, A., 2004, "Physical Modelling and Similitude of Air Bubble Entrainment at Vertical Circular Plunging Jets," *Chem. Eng. Sci.,* Vol. 59, pp. 747-758.
[6] Cummings, P.D., and Chanson, H., 1999, "An Experimental Study of Individual Air Bubble Entrainment at a Planer Plunging Jet," *Chem. Eng. Research and Design*, Trans. IChemE, Part A, vol. 77(A2), pp. 159-164.
[7] El Hummoumi, M., Achard, J. L., and Davoust, L., 2002, "Measurements of Air Entrainment by Vertical Plunging Liquid Jets," *Experiments in Fluids*, Vol. 32, pp. 624-638.
[8] Kusabiraki, D., Niki, H., Yamagiwa, K., and Ohkawa, A., 1990, "Gas Entrainment Rate and Flow Pattern of Vertical Plunging Liquid Jets," *Can. J. Chem. Engg.*, Vol. 68, pp. 893-903.
[9] McKeogh, E.J., and Ervine, D.A., 1981, "Air Entrainment Rate and Diffusion Pattern of Plunging Liquid Jets," *Chem. Eng. Sci*., Vol. 36, pp. 1161-1172.
[10] Michel, J. M., 1984, "Some Features of Water Flows With Ventilated Cavities," *Fluids Engg.* Trans. ASME, Vol. 106, pp. 319-326.
[11] Robertson, D. D. C., O'Shaughnessy, D. P., and Molloy, N. A., 1973, "The Mechanism of Sheath Formation by Plunging Liquid Jets," *Chem. Eng. Sci.*, Vol. 28, pp. 1635-1636.